

A HIGH-POWER TI:SA LASER SYSTEM FOR
ATOMIC QUANTUM WALKS EXPERIMENTS

MASTERARBEIT IN PHYSIK

VON

KARTHIK KRISHNAPPA CHANDRASHEKARA

angefertigt im
Institut für Angewandte Physik

vorgelegt der
Mathematisch-Naturwissenschaftlichen Fakultät
der
Rheinischen Friedrich-Wilhelms-Universität Bonn

im
January 2020

1. GUTACHTER:
Prof. Dr. Dieter Meschede

2. GUTACHTER:
Prof. Dr. Stefan Linden

ABSTRACT

This thesis details the experimental efforts towards quantification of laser frequency noise by the use of an optical frequency discriminator and its suppression by means of measuring and reducing optical path length differences to prevent heating and loss of ultracold Caesium atoms trapped in two-dimensional state-dependent optical lattice. The discriminator used is a Fabry-Perót cavity with the side-of-fringe locking technique to be sensitive to frequency fluctuations of the input light field which are detected as changes in the intensity of the cavity signal. The measured noise spectrum revealed the performance of the laser in the frequency domain and was used to refine the same. A reduction in the laser linewidth was achieved in this manner. The same cavity was also transformed in to a transfer cavity to prevent long-term drift in the laser frequency. The frequency noise cannot be completely eliminated from the laser and so the task then became the reduction of the optical path length differences in the experiment by which the noise can manifest at the position of the atoms. Conditions for achieving minimal path length differences were derived. Three methods were employed to measure the path length differences: A geometric distance measurement, an optical measurement using interferometry and at last using the atoms. The use of the atoms in particular displayed the extent to which the common-mode frequency noise can influence the experiment.

CONTENTS

INTRODUCTION	1
1 A 2-D QUANTUM SIMULATOR	3
1.1 Optical lattices	3
1.2 Ultracold atoms on a 2-D lattice	5
1.2.1 Trapping, manipulation and transport of cold Caesium atoms	6
1.2.2 Quantum walks	9
1.3 Factors limiting coherent control	11
1.3.1 Decoherence mechanisms	12
1.3.2 Laser noise as a source of decoherence	14
2 TI:SA LASER SYSTEM	19
2.1 Hardware in use	19
2.2 Laser intensity noise	22
2.3 Intensity noise in optical fibres	23
2.3.1 Photonic Crystal fibres	25
2.4 Laser frequency noise	26
2.4.1 Optical resonators	26
2.4.2 Construction of a high finesse Fabry-Perót cavity	29
2.4.3 Measurement of frequency noise	34
2.4.4 Estimation of laser linewidth from frequency noise	36
2.5 Feedback control via transfer cavity	40
3 EQUALISATION OF OPTICAL PATH LENGTHS	43
3.1 Conditions for equalisation	43
3.1.1 Constraint equations	46
3.2 Measurement of optical path lengths and differences	48
3.2.1 Geometric measurement	48
3.2.2 Optical measurement through FMCW interferometry	48
3.2.3 Measurement using atoms	52
OUTLOOK	57
A APPENDIX	59
A.1 Principle of optical FMCW interferometry	59
BIBLIOGRAPHY	61
ACKNOWLEDGEMENTS	65
DECLARATION	67

INTRODUCTION

Any attempt to understand a complex quantum system involving many-body interactions [1, 2] beyond simplifying assumptions starts with the need for a simulation of the same with an equivalent system. This for the simple reason that classical computation fails in the face of the large Hilbert space involved whose dimension scales exponentially with the number of particles [3, 4]. For instance, it takes 2^N bits to store the states of N spin-1/2 particles and a further 2^{2N} bits to track their time-evolution with the associated computational time being also on the order of 2^{2N} . This explosion in required memory and time can be overcome with a quantum system tuned to emulate the dynamics of the system of interest. With information now encoded in *qu*-bits or quantum bits, a Hilbert space of dimension 2^N then needs only N qubits to fully span the space of states. This array of qubits can then be driven along an arbitrary trajectory in the state space through a series of unitary transformations determined by single or a set of specific local Hamiltonians. Known as a *Quantum Simulator* in the common parlance of the field of study, such a system becomes the necessary foundational architecture for further inquiry into more complex physical processes.

There are many platforms available today that as a result of the high degree of control are all viable options for realizing quantum simulators depending on the type of problem they seek to solve of which cold, neutral atoms trapped in an optical lattice is one [5]. Other platforms such as Trapped Ions [6] or Solid-state systems [7] (Also, photons [8, 9], quantum dots [10] and NV centers [11]) come with certain immediate advantages such as scalability but also have their own unique challenges. Although trapped atoms as a platform is no exception, is relatively simpler to implement and is grounded in a long, deep understanding of Atom-Light interaction [12].

The use of the optical dipole force to trap atoms starting with the breakthrough of Chu et al. (1986) triggered a cascade of such experiments [13]. First used to increase the efficiency of some methods of optical cooling, interfering counter-propagating, far-detuned laser light to generate spatially periodic, conservative potential wells - an optical lattice - is now a standard technique to confine an ultracold ensemble of atoms through electric dipole interaction. Among the various quantum optical applications that this has given rise to, one is as an investigative tool to probe the rich, exotic zoo of quantum matter the possibility of which is speculated in Condensed Matter Theory through the perspective of topology [14]. Prompted in such a direction are the experiments in Bonn where the objective is to exploit another phenomenon that is Discrete-Time Quantum Walks (DTQW) [15], the quantum analogue of the classical random walk, to simulate a certain class of Hamiltonians periodic in time allowing for the experimental realization of novel topological phases [16, 17]. For this, individual, neutral, ^{133}Cs atoms with pseudo-spin 1/2 are delocalized in a state-dependent optical lattice with the qubit encoded in two long-lived hyperfine ground states corresponding to spin-1/2 up and down. Implemented on an one-dimensional (1-D) lattice, efforts are currently underway to realize quantum walks on a two-dimensional (2-D) lattice.

To the experiment, the optical lattice offers in itself its most central tool and in doing so, presents one of the experiment's most fundamental technical limits. Ideally, the light

field that is used to generate the lattice would need to have no adverse influence and the device from which it is sourced be infinitely tunable but since that rarely is the case, it falls on the user to determine the extent of the flexibility available. This thesis will describe such an attempt with regard to the Titanium-Sapphire (Ti:Sa) lasers in the 2-D DTQW experiment. The two lasers whose characterization and integration in to the experiment will be described in the following pages, were newly obtained as an upgrade over an earlier single Ti:Sa laser that was in use for the following chief reason - A high power laser beam is critical to the setup in order to trap atoms in a deep trapping potential (with a depth > 1 mK) over a large spatial volume. This prevents the individual atoms from hopping to neighboring sites in the lattice which would result in the loss of fine control of a system designed to deterministically transport and image atoms. The lasers though can come with inherent fluctuations in their intensity or possess instability in frequency that can heat the atoms out of the lattice limiting the coherence times and so quantifying this noise can be invaluable for understanding the limits imposed on the experiment. It is not enough though that we quantify the noise but also work toward curtailing it for which we need to identify the manner in which the noise manifests. This will form the core of the work presented here with a special focus on laser frequency noise and the optical path length differences which magnify its effect.

OUTLINE

This thesis is divided into three chapters: Chapter one will begin with an elucidation of the fundamental scientific principles upon which the two-dimensional discrete-time quantum walk experiment rests followed by a description of the current experimental setup, the concept of decoherence and its causes with special focus on intensity and frequency noise. Chapter two is dedicated to describing the laser devices in use in the experiment in terms of its layout and function before detailing the methods used to measure intensity and especially frequency noise with the build and use of an optical resonator the utility of which was extended from that as a measurement device to a transfer cavity for actively stabilising the laser used to generate the lattice against frequency drifts as will explained in the closing section. The chapter will also include a note on intensity noise in optical fibers when large powers are coupled in to them with the solution being large mode area fibers such as Photonic Crystal Fibers (PCF) due to be installed for use in the experiment. The final chapter will deal exclusively with optical path lengths differences, explaining their role in enhancing the frequency noise and presenting methods used to measure the path length differences in the experiment. Towards the end, an outlook will serve to outline present understanding and future directions for the formal conclusion of the work presented here.

The basis for a quantum simulator that we shall consider here is the optical lattice - a dipole potential with a periodic structure engineered to trap an ensemble of atoms and allow for their manipulation. We shall start with some basic theory regarding dipole potentials and the realisation of an optical lattice before describing the 2-D DTQW experiment in sufficient detail. The chapter will end with a look in to a complication that arises in all such experiments, namely, decoherence. The mechanisms by which it intrudes in to the experiment will be listed, two of which - intensity and phase noise - discussed in more detail as they bear relevance to the subsequent investigation.

1.1 OPTICAL LATTICES

The incidence of an oscillating electric field \mathbf{E} on atom induces in it a time-dependent dipole moment. When suitably off-resonant, the driving field does not cause any transitions in the atom but has the dipole moment \mathbf{d} follow its oscillations and is then given by,

$$d_i = \alpha_{ij} E^j \quad (1.1)$$

where α is the complex atomic polarizability tensor which depends on the driving frequency and the energies of the non-resonant excited states of the atom. When the driving frequency is close to one of the transition frequencies, it results in what is called the *AC Stark Effect* which is a shift in the energy levels proportional to,

$$\delta E = -d_i E^i = -\alpha_{ij} E^j E^i \quad (1.2)$$

For isotropic media for which the polarizability is a scalar and taking in to account that only the real part of the polarizability which is the in-phase component responsible for the dispersive properties of the interaction, the AC shift can be rewritten as,

$$\delta E = -\text{Re}(\alpha) I \propto \frac{I}{\Delta} \quad (1.3)$$

where $I = |\mathbf{E}|^2$ is the field intensity and the polarizability becomes inversely proportional to the difference between the driving and the transition frequency called the detuning Δ (The exact expression for the shift can be arrived at by second-order time-independent, non-degenerate perturbation theory with the form of the polarizability also obtained by considering a two-level system interacting with a classical radiation field and are both more insightful exercises). The atoms therefore feel an optical potential that follows the spatial intensity pattern with the sign determined by the detuning. This interaction

potential is the reason behind the *dipole force* \mathbf{F} which is given as the gradient of the potential,

$$U = \delta E \propto \frac{I}{\Delta} \quad (1.4a)$$

$$F_\mu = -\partial_\mu U \propto -\frac{\partial_\mu I}{\Delta} \quad (1.4b)$$

As is evident, the characteristic of the force is conditioned on the gradient of the intensity of the light field and the detuning - The force is directed towards the intensity maxima which corresponds to potential minima for red-detuned light ($\Delta < 0$) with the force directed away from the intensity maxima for blue-detuned light ($\Delta > 0$). Additionally, keeping in mind that the scattering rate scales as I/Δ^2 , a typical trapping potential is constructed by the interference of counter-propagating laser beams of the same wavelength and polarisation with high enough intensities and large detunings.

The optical lattice is one such trapping potential, a standing wave that is a spatially periodic potential for atoms that is of the form,

$$U_1 = U_o \cos^2(k_1 a^1) \quad (1.5)$$

written here using the plane-wave approximation for the one-dimensional case at some point a^1 along the e_1 -direction with the depth of the optical lattice given by U_o which is proportional to the intensity of the beams, the magnitude of the wave vector along this direction by $k_1 = 2\pi/\lambda$, where λ is the wavelength of the light.

Being defect-free and rigid, optical lattices are nearly ideal, periodic optical potentials with the added benefit of the degree of control they offer. This control comes in various forms as tunable parameters such as lattice geometry, tunneling rates, on-site and nearest neighbor interactions or special potentials which can be applied on the atoms all in low temperature regimes and differing time scales. It is this flexibility on offer that we shall exploit to put together our quantum simulator and induce certain dynamics (Figure 1.1).

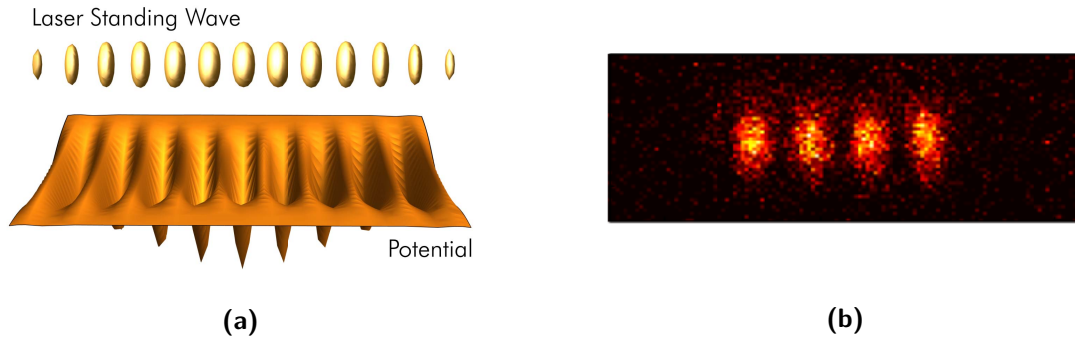


Figure 1.1: (a) Periodicity is another key property of the optical lattice which is $\lambda/2$ given the wavelength λ of the interfering laser beams. (b) A fluorescence image of atoms trapped in a 1-D optical lattice (Image taken from [18]).

1.2 ULTRACOLD ATOMS ON A 2-D LATTICE

In a one-dimensional lattice we are already provided with a robust tool to probe diverse quantum phenomena. In an earlier work, the 1-D DTQW experiment was first used to demonstrate quantum walks. This was then used to simulate the effect of electric fields on the charged particles in lattice potentials [19] and also observe a violation of the Leggett-Garg inequality [20]. The experiment has many more possibilities and work continues in those directions. A natural extension of the system to consider though would be a two-dimensional lattice. With such a system comes the promise to re-create, by carrying out quantum walks again, a topological insulator that only in two dimensions and above shows distinct spatial boundaries between regions with disparate topological phases and topologically-protected edge states so called because they exist along these boundaries [21]. In an age where topological insulators are sought after in an effort to build solid-state devices with little to no dissipation [22, 23], cold atom systems offer a convenient route to the same bypassing the challenges offered in their synthesis in electronic systems and more immediately, serve as means to understand the underlying complexity.

The two-dimensional optical lattice is created by the addition of a beam on the same horizontal plane in a direction orthogonal to the two counter propagating beams. The lattice can therefore be thought of as the sum of two one-dimensional potentials with each of the counter-propagating beams interfering with the orthogonal beam creating regions of modulated intensity at 45° to the respective wave vectors (Figure 1.2),

$$I_{ij} = I_o \cos^2\left(\frac{1}{2} k_l \mathbf{e}^l \cdot (a^i \mathbf{e}_i \pm b^j \mathbf{e}_j)\right) \quad (1.6)$$

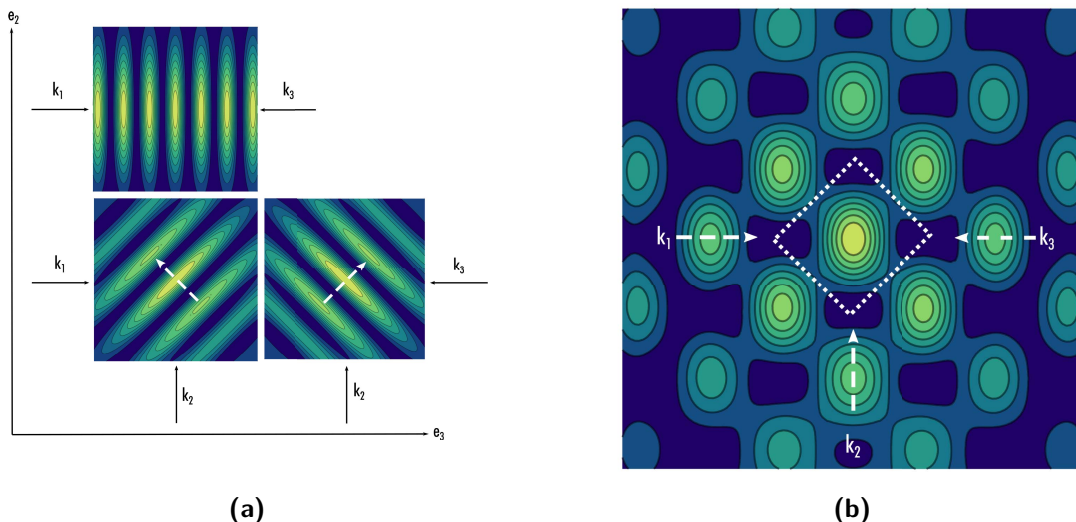


Figure 1.2: (a) The top left image is the one 1-D lattice formed by two counter propagating (Gaussian) beams here along e_3 with $k_3 = -k_1$. Adding the orthogonal beam along e_2 creates an interference pattern along the $\frac{1}{\sqrt{2}}(0, 1, \pm 1)$ vector for each of the two other beams as shown here in the bottom. (b) Summing up the resulting two 1-D potentials gives the desired 2-D lattice potential with its discrete sites denoted by the bounding box.

1.2.1 Trapping, manipulation and transport of cold Caesium atoms

Having constructed the 2-D lattice in such a manner, it then becomes necessary to design a scheme to utilize it as a trap for atoms. It starts with the atoms being first collected in a Magneto-Optical Trap (MOT). In the most commonly used geometry for a MOT, three pairs of red-detuned circularly polarized beams are aligned mutually perpendicular to each other and directed at some atomic vapour at the center of a quadrupole field generated by a set of coils in the anti-Helmholtz configuration in a chamber that is kept at low pressure to reduce background gas collisions. The atoms then experience a force as a result of the imbalance in the radiation pressures of the six beams which arises due to a combination of the Doppler and the Zeeman effect. An atom moving towards an incoming beam will see light that is Doppler shifted in to resonance in its rest frame and so will absorb and scatter off a photon thereby losing momentum. This occurs repeatedly over multiple cycles and in all directions resulting in the cooling of the atom. In addition, the spatially inhomogeneous magnetic field will result in a corresponding spatially variable shift of the hyperfine sublevels of the atom which are consequently no longer degenerate. This shift linearly increases radially away from the zero of the field. The circularly polarized light comes in to resonance with these different Zeeman states depending on its helicity for the on-axis and off-axis cases which again produces a restoring force due to photon recoil, arresting its motion. In this experiment involving Caesium, laser light near-resonant with the D_2 line is shined to cycle the atoms in a closed transition with a repumper beam to counteract the occasional off-resonant scattering that send the atoms out of the cooling transition and in doing so reach a Doppler-limited temperature of $125 \mu\text{K}$. The cloud of atoms that forms is then to be loaded on to the 2-D lattice but only so after supplementary cooling by an optical molasses that uses polarisation gradients [24] which further reduces the temperature to within tens of microkelvins. At this potential depth, the trapped atom is well approximated by the harmonic oscillator model [13]. The quantized vibrational energy levels of the atom are then given in terms of a trap frequency ¹ ω_{tr} as $(n + 1/2)\hbar\omega_{tr}$. These energy levels represent the temperature of the atom, with a hotter atom occupying the higher vibrational levels. This conception is therefore useful in describing heating effects in the experiment (see Section 1.3.2).

State-dependent trapping

To actually trap the atoms in the lattice, we make use of the energy level structure of the atoms to produce a spin-dependent trapping force. For Caesium, the D1 transition from the ground state Zeeman sublevel $^2S_{1/2}$ to the excited state sublevel $^2P_{1/2}$ is of the wavelength 894.6 nm while the D_2 transition from the same ground state sublevel to the other excited state sublevel $^2P_{3/2}$ is of the wavelength 852 nm [25]. By choosing the wavelength of the light generating the lattice to lie between the two excited state sublevels with $m_J = \pm 1/2$, considering the light would be red-detuned for $^2P_{3/2}$ and blue-detuned for $^2P_{1/2}$, the dipole force would be attractive for one and repulsive for the

¹ This is slightly more complicated in the 2-D case where there are *two* trap frequencies: ω_{tr} and the second, due to elliptic distortion caused by the three beam setup, given by, $\omega_{tr}/\sqrt{3}$

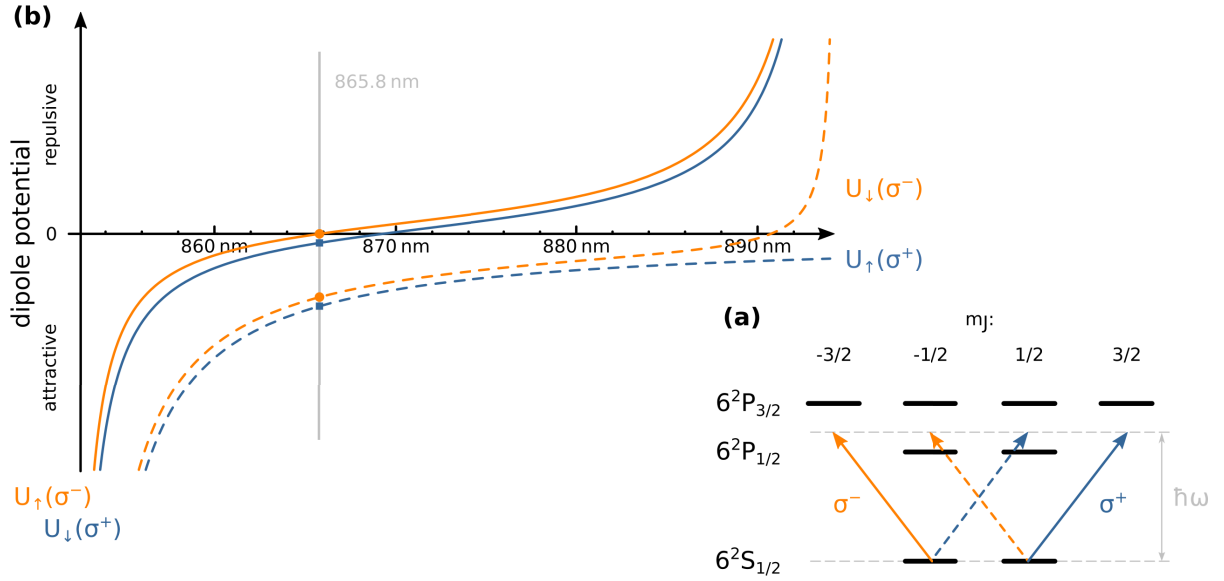


Figure 1.3: (a) Fine structure splitting in the ground and excited states of Caesium. (b) The exact potentials for each of the qubit states (see *State manipulation*) for the two circular polarisations can be calculated by the reduction of the dipole matrix elements of the total angular momentum using the Wigner-Eckart Theorem [26]. These potentials have an implicit dependence on the wavelength seen here for values between the D-line doublet (852 and 894 nm). The wavelength for which the combination of polarisation and states give attractive potentials and the opposite combination of which has no effect can be singled out: 865.8 nm (Image taken from Brakhane [27, p. 68])

other, effectively cancelling each other. Furthermore, if the beams are circularly polarized, each ground state which due to spin-orbit coupling is given by,

$$\begin{aligned} |+\rangle &= |J = 1/2, m_J = +1/2\rangle \\ |-\rangle &= |J = 1/2, m_J = -1/2\rangle \end{aligned} \quad (1.7)$$

is exclusively influenced by σ^+ and σ^- respectively (Figure 1.3(a)) as qualified by a quantisation axis defined by the magnetic field vector of a guiding field here oriented along the two counter-propagating lattice beams. Incorporating the additional interaction with the nuclear spin in the presence of this magnetic field that causes hyperfine splitting and calculating the dipole potentials for the two polarisation components and the corresponding hyperfine levels formed from the $^2S_{1/2}$ ground state fine structure (more under *State manipulation*), the characteristic wavelength was determined to be 865.8 nm and is referred to as the "magic" wavelength (Figure 1.3(b)). This paves the way for state manipulation and our novel state-dependent transport of the atoms trapped in the lattice.

State manipulation

The hyperfine splitting of the $^2S_{1/2}$ ground state presents with us with a convenient basis to encode our qubit in for carrying out coherent manipulations on, being long-lived and also at 9.2 GHz apart, can be coupled by microwave radiation. The hyperfine substructure of the energy levels is formed by the interaction of the atom's nuclear spin I with the sum of its orbital angular momentum and spin angular momentum denoted

as J in an external magnetic field. For Caesium with $I = 7/2$, this gives us as the two outermost states,

$$\begin{aligned} |\uparrow\rangle &= |F = 4, m_F = 4\rangle \\ |\downarrow\rangle &= |F = 3, m_F = 3\rangle \end{aligned} \quad (1.8)$$

which forms our pseudo spin-1/2 system. These states however cannot both be addressed with a single pure circular polarisation component each as is evident when the above states are rewritten in the fine structure basis,

$$\begin{aligned} |\uparrow\rangle &= |I = 7/2, m_I = 7/2\rangle \otimes |+\rangle \\ |\downarrow\rangle &= \sqrt{\frac{7}{8}} |I = 7/2, m_I = 7/2\rangle \otimes |-\rangle - \sqrt{\frac{1}{8}} |I = 7/2, m_I = 5/2\rangle \otimes |+\rangle \end{aligned} \quad (1.9)$$

The $|\downarrow\rangle$ state carries some sensitivity to the σ^+ polarisation owing to the fact that it is a differentially weighted superposition of the two ground states while the $|\uparrow\rangle$ state has no such contribution from the other state and so is decoupled from the σ^- polarisation. More intuitively, the potentials for the two states as shown earlier in [Figure 1.3\(b\)](#) showing this "crosstalk" written down are,

$$\begin{aligned} U_{\uparrow} &= U_{\sigma^+} \\ U_{\downarrow} &= \sqrt{\frac{7}{8}} U_{\sigma^-} - \sqrt{\frac{1}{8}} U_{\sigma^+} \end{aligned} \quad (1.10)$$

But regardless of the lack of wholly distinct potentials for the two atomic species, an optical lattice of left and another of right circular polarisation should, in principle, permit individual control of the absolute position of the atoms in the trapping region.

State-dependent transport

Drawing from previous realisations [28–30] of state-dependent transport, the implementation in first the 1-D and later in the 2-D DTQW experiment improves upon them by the use of a novel high-precision, large bandwidth polarisation synthesizer [31] that offers greater adjustability going beyond just relative shifting of the two spin components by only at most one lattice site to enabling atom repositioning to within 1 Å. This was done by building on the concept discussed previously of having independent optical lattices with orthogonal circular polarisation to trap the two spin states and adding the ability to translate the lattice by changing the phase of the interfering light fields. This has allowed from atom sorting to obtain low entropy ensembles of atoms [18] to quantum walks [15, 20].

Synthesis of the polarisation is carried out on the counter-propagating beams which can re-imagined as,

$$\begin{aligned} E_1 &= \frac{1}{\sqrt{2}} (E_{\uparrow} e^{i\theta_{\uparrow}} \mathbf{e}_{\sigma^+} + E_{\downarrow} e^{i\theta_{\downarrow}} \mathbf{e}_{\sigma^-}) e^{ik_i x^i} \\ E_3 &= \frac{1}{\sqrt{2}} (E_{\uparrow} e^{i\phi_{\uparrow}} \mathbf{e}_{\sigma^+} + E_{\downarrow} e^{i\phi_{\downarrow}} \mathbf{e}_{\sigma^-}) e^{ik_i x^i} \end{aligned} \quad (1.11)$$

with amplitude $E_{\uparrow,\downarrow}$, phases as $\theta_{\uparrow,\downarrow}, \phi_{\uparrow,\downarrow}$ and the Jones vector for circular polarisation $\mathbf{e}_{\sigma\pm} = \frac{1}{\sqrt{2}}(1, \pm i, 0)$. Light in one direction interferes with light of the same circular polarisation from the opposite direction and like detailed before with the third perpendicular beam which is only linearly polarized and can be thought of as a reference beam forming the 2-D lattice. More accurately, they form a 2-D optical "superlattice" with two separate, overlapping sub-lattices made of light of different circular polarisations.

As can be easily pictured in the 1-D case, a phase-shift in either one of the interfering beams causes a translation of the standing wave potential with a change of over the full range of 2π corresponding to a translation by $\lambda/2$ which is one lattice site. The same is possible in the 2-D case by keeping a constant phase difference with the reference beam and changing the phase of the other beams to move the lattice by one site, which has now the extent of $\lambda/\sqrt{2}$, along the diagonals -

$$\begin{aligned} \text{Shift along } \frac{1}{\sqrt{2}}(0, 1, +1) &= \frac{\lambda}{\sqrt{2}} \frac{\theta_{\uparrow,\downarrow}(t)}{2\pi} \\ \text{Shift along } \frac{1}{\sqrt{2}}(0, 1, -1) &= \frac{\lambda}{\sqrt{2}} \frac{\phi_{\uparrow,\downarrow}(t)}{2\pi} \end{aligned} \quad (1.12)$$

By ramping the phase of only one of the polarisation components for equal amplitudes of the synthesized beams, only one of the two sub-lattices can be moved and so only one of the two states of the trapped atoms it confines (Figure 1.4(a)). A combination of two phase shifts facilitates arbitrary trajectories of transport for the lattice (Figure 1.4(b)). This is practically made possible by the use of acousto-optical modulators with which each individual trap beam is controlled in terms of both amplitude and phase, stabilised by intensity and optical phase lock loops [32].

1.2.2 Quantum walks

The schema to trap and transport atoms in the 2-D DTQW experiment was designed for the core objective of executing quantum walks. First proposed by Feynman in his checkerboard model [33], the quantum random walk is similar to its classical analogue but in contrast to it, the randomness arises due to the now predominant quantum nature of the walker. Instead of definite states as the classical walker will be found in and an external probabilistic event like a coin flip determining the direction of the step, the quantum walker is in a coherent superposition of states and every step is a unitary evolution of the walker with any measurement of the internal state being destructive. The stochasticity is therefore inherent. The walker, which can be thought of as a wave function, as it progresses undergoes multi-path interference which spreads the probability distribution (Figure 1.5(a)) ballistically with $\mathcal{O}(n)$ where n is the number of time steps as opposed to the classical scenario where it goes more slowly as $\mathcal{O}(\sqrt{n})$ [34]. Quantum walks can so in principle offer a polynomial or in some cases even exponential speed up in algorithms that employ randomisation [35].

The 2-D DTQW experiment aims to carry out quantum walks in position space over discrete time steps with the walkers being the cold, neutral Caesium atoms in the 2-D optical lattice. The walk starts with a *coin* operation which sends the atom in to a coherent superposition of the qubit states, $|\uparrow\rangle$ and $|\downarrow\rangle$ (as introduced in eq. 1.8), achieved by means of microwave radiation that resonantly couples the two states. This is followed by a *shift*

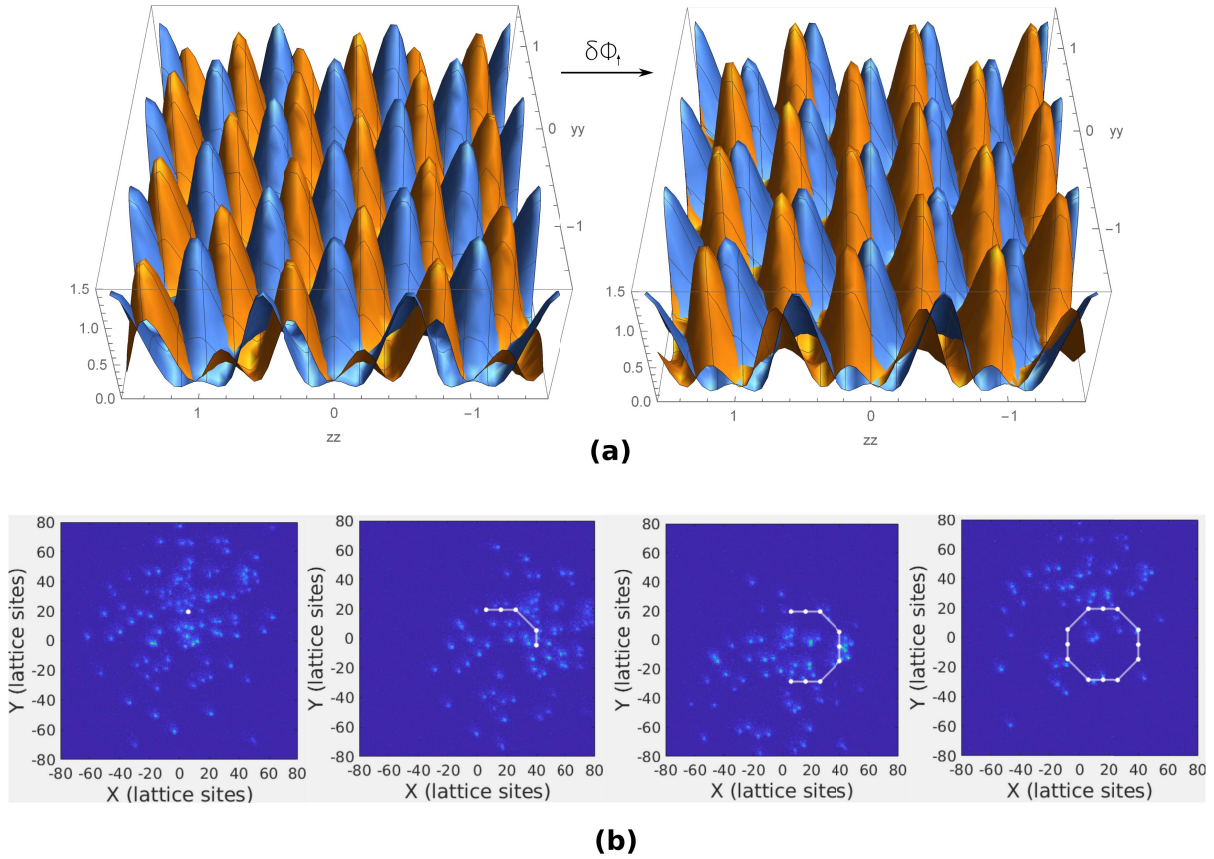


Figure 1.4: (a) *State-dependent transport* - Changing the phase of one of the polarisation components in one arm shifts a sub-lattice as can be visualised here with the sub-lattice shown in orange moving across $\frac{1}{\sqrt{2}}(0, 1, -1)$ vector since only the right circular polarisation component of the HDT3 beam coming from the right $((0,0,-1)$ direction) was varied with respect to the HDT2 beam coming from below $((0,1,0)$ direction). (b) *State-independent transport* - Changing the phases in a certain sequence can be used to trace very specific paths like one in the shape of a hexagon shown here with actual atoms. Since only two phases for the opposite polarisations were varied, all atoms irrespective of their internal state are moved.

operation by state-dependent transport which moves the atom by one lattice site in a direction that is subject to the spin state. Iteratively applying the two operations would mean the atomic wave function splits and spreads over multiple trajectories producing the interference and the associated distribution of the position of the atoms across the lattice. For this, it is essential that the transport operation is as fast as it can be without creating excitations that can decohere the superposition and reduce the interference contrast. This necessitates the use of optimal control [36] with methods like *bang bang* being used for atom transport [37]. The number of steps taken too is limited by decoherence caused by light shifts that can be overcome to a degree with resolved sideband cooling to the 3-D vibrational ground state [38]. This is currently at its initial level of implementation in the 2-D experiment and needs to be optimized before attempting quantum walks with optimal control transport which remains an endeavour for the future.

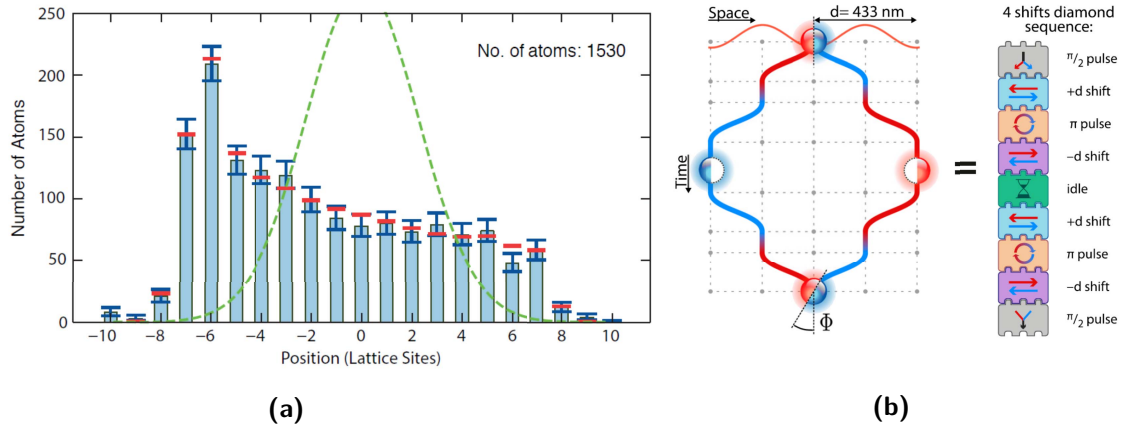


Figure 1.5: (a) Caesium atoms after a 20-step quantum walk show a skewed distribution as opposed to the classical random walk distribution shown here in as a dashed line. A theoretical model that assumes a 5% loss of coherence per step predicts a distribution (represented as horizontal lines) that agrees well with the experimental data (in blue) (Image taken from [38]). (b) The atom interferometer is operated by alternating spin rotations and spatial translations which altogether resembles a diamond in space-time (Image adapted from [39]).

Planned upcoming experiment: Single Atom Interferometer in 2-D

One of the more immediate goals of the 2-D DTQW experiment is the set up of a single atom interferometer, which like the quantum walks, has been shown to be practically realisable in the 1-D DTQW experiment [39]. A tightly localized single atomic wave function is prepared in a superposition of its spin states before being split and transported along two spatially separate paths and then recombined. The accumulated phase difference as a result of this transport is then extracted by a Ramsey probe [40]. Such an interferometer has been used for precision measurements such as that of external forces on atoms with the promise of being an effective tool to detect the Casimir-Polder force or demonstrate the Sagnac effect. In the 1-D experiment, the interferometer was operated by translating the delocalized wave function back and forth in the polarisation synthesised lattice in a geometry that resembles a diamond in space-time (Figure 1.5(b)) along with a variation of the same. The addition of an extra degree of freedom with the second spatial dimension in the 2-D experiment should allow for more complicated geometries which would be of great interest. Also, the interferometer mode of operation resembles part of the same for quantum walks and is therefore a highly relevant stepping stone.

However, in all these experiments involving coherent manipulations, the challenge of decoherence looms large and so it becomes crucial to identify, quantify and to counteract any physical mechanisms responsible. The task starts with knowing and learning of the myriad sources of decoherence.

1.3 FACTORS LIMITING COHERENT CONTROL

There are no known quantum systems in the mesoscopic and further to the macroscopic limit which are completely decoupled from external degrees of freedom termed as their

environment. Imperfect isolation renders the system unable to maintain its coherence indefinitely causing an evolution of the system from a pure quantum state into a statistical mixture of states. Its dynamics can no longer be treated as unitary and reversible. The causes for what is a loss of information to its surroundings are the fundamental limiting factors of any experiment involving such a system with the 2-D DTQW being no exception. Phenomenologically, this decay of coherence can be introduced as damping terms in the optical Bloch equations describing the dynamics of a two level atom interacting with an external field,

$$\begin{aligned}\langle \dot{u} \rangle &= \delta \langle v \rangle - \frac{\langle u \rangle}{T_2} \\ \langle \dot{v} \rangle &= -\delta \langle u \rangle + \Omega_R \langle w \rangle - \frac{\langle u \rangle}{T_2} \\ \langle \dot{w} \rangle &= -\Omega_R \langle v \rangle - \frac{\langle w \rangle - w_{st}}{T_1}\end{aligned}\tag{1.13}$$

with δ being the detuning, Ω_R the generalised Rabi frequency, T_1 the longitudinal relaxation time and T_2 the total inhomogeneous transverse decay time. The ensemble averages of the components of the so-called Bloch vector are written here with w being the difference in populations each of which is found as elements of the main diagonal of the density matrix of the two level system while u is twice the real part of the sum of the off-diagonal elements (redefined with a phase determined by the detuning) which are called the coherences representing the system response at the driving frequency and v is twice the imaginary part of the their difference.

The longitudinal relaxation time T_1 gives the time in which the population difference decays to a stationary value w_{st} as governed by off-resonant scattering of photons from the lattice beams for instance. This can bring about a transition out of the two-level system which puts an upper bound on the lifetime of the qubit states. A full suppression requires changing the wavelength of the light or reducing the dipole potential by lowering the intensity both of which are unfeasible. On the other hand, the total homogeneous transverse decay time T_2 is given by the polarization decay time T_2' and the reversible dephasing time T_2^* as,

$$\frac{1}{T_2} = \frac{1}{T_2'} + \frac{1}{T_2^*}\tag{1.14}$$

The reversible inhomogeneous dephasing T_2^* occurs because the resonant frequencies are shifted for the many atoms across the ensemble due to the interaction with the environment. This can cause the Bloch vectors of each atom to precess with different angular velocities and so go out of phase relative to each other (Figure 2.1). This dephasing can ultimately be corrected for by techniques such as spin echo [41] but the homogenous dephasing is difficult to correct for at anywhere but the source.

1.3.1 Decoherence mechanisms

Decoherence has several physical origins in the DTQW experiments all of which have been discussed in detail previously [43]. A quick overview of the same with the latest developments can lead us to the principal focus of this thesis.

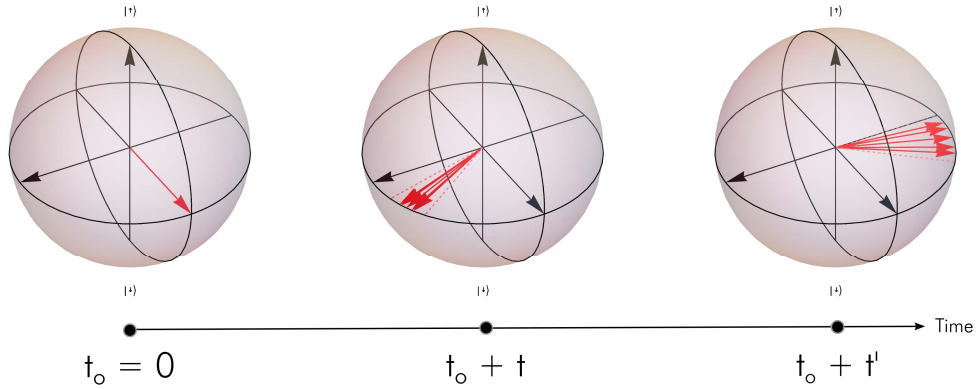


Figure 1.6: Over the evolution of a quantum system, interaction with the environment can push the elements of the system out of sync with each other in what is called dephasing. Each element, represented by a vector in the Bloch sphere [42] shown here of an atom prepared in a superposition of the two possible states, picks up a different phase.

The shifts in the resonance frequencies of the two spin states can be caused by scalar *differential light shift* that is directly proportional to the laser intensity and inversely so with the detuning. There is also its vectorial counterpart determined by the ellipticity of the polarisation or imbalance in power between the two polarisations used for the synthesised lattice. One cause of the ellipticity of the polarisation is known to be birefringence of the material of the ultra-high vacuum glass cell that sits inside the science chamber within which the atoms are trapped. Despite the glass being designed to be of low birefringence in the 2-D experiment, an induced vectorial light shift was recently detected though the effect was certainly smaller by an order of magnitude compared to the same in the 1-D experiment which lacks this type of glass cell. It was also demonstrated that this vectorial light shift could be compensated for by the scalar light shift with a noticeable improvement in the measured coherence times of atoms in free fall.

Fluctuations in the guiding magnetic field originating in the driving current can be responsible for spin decoherence, with the same being caused to a smaller extent by noise in the gradient magnetic field that can also bring about position-dependent dephasing. With stabilisation of the currents driving the coils being carried out and a Mu-metal shielding around the science chamber to cut out any additional external magnetic fields, their adverse effect has been largely stamped out in the 2-D DTQW experiment. A new investigation using Ramsey interferometry that involved sitting on a point on the Ramsey fringe by fixing the microwave pulse phase, it was found that the shot-to-shot magnetic field fluctuations in terms of frequency shifts for the same Ramsey duration over several runs had an RMS spread of around 30 Hz which being small enough is well within requirements.

The potential crosstalk (eq. 1.10) leads to a modulation of the potential depth for the $|\downarrow\rangle$ states which can heat them out of the lattice. This *motional excitation of atoms during transport* can be curtailed by optimising the transport phase ramp shape that will be implemented. In the same setup for transport, maintaining high polarisation

purity and damping out polarisation jitter of the synthesized beams also is essential. This has been largely dealt with by the use of high precision optics and practices such as polarisation maintainance extracting extinction ratios that are in the order of 10^{-5} . Pointing instabilities that refer to beam orientation can similarly cause trap depth modulation, change lattice geometry but considering the extensive temperature control of the laboratory environment and limited mechanical vibrations of the optical tables, this is of little concern.

Spontaneous scattering of lattice photons can induce recoil heating of the atoms with the elastic type called Rayleigh scattering causing pure spin dephasing while the inelastic type called Raman scattering mixes spin populations. In the same vein, collisions with the background gas limits lifetimes.

1.3.2 Laser noise as a source of decoherence

Of the many ubiquitous sources, the noise from the laser used to cool and trap the atoms can be very significant in its presence and influence. The noise finds its roots in the core functioning of the laser device which, depending on the control on offer, can be dealt with in situ or is a brick wall that requires going around by means of external noise suppression. This demands inspection and we start by identifying two types of noise that we can attribute to the laser - Intensity and Frequency Noise.

Intensity Noise

Fluctuations in the intensity of the laser can be due excess noise in the pump source which could be noise in the current driving the pump as is usually the case if they are diode lasers, relaxation oscillations in the gain medium because of changes in the pump power causing the output power of the pumped laser reach a steady state only after some initial transient oscillations or thermal fluctuations within the gain medium. Cavity losses which is a combination of losses at mirrors which are not perfectly reflective, scattering in the beam path and diffraction losses are all not constant over time and so can also be responsible for the noise.

Whatever the origins, it is clear that the abrupt changes in the laser intensity causes the modulation of the lattice depth. This heats the atoms out of the trap and so we would like to know how long we can hold on to atoms, choosing to tackle the noise if this time not long enough. The calculation of heating times made possible with first-order time-dependent perturbation theory should give us an estimate of the limit we have with regard to storage times of the atoms [44]. The heating rate is given by the transition rates between the vibrational states of the trap separated by energies expressed in terms of the trap frequencies.

We start with the Hamiltonian for Caesium with mass m_{Cs} trapped in a one dimensional lattice potential,

$$H = \frac{p^2}{2m_{Cs}} + \frac{1}{2} m_{Cs} \omega_{tr}^2 x^2 \quad (1.15)$$

The spring constant, tucked away in the trap frequency $\omega_{tr}^2 = k_o m_{Cs}^{-1}$, is proportional to the time averaged laser intensity I_o and exhibits a fractional change $\epsilon(t) = \frac{I(t)-I_o}{I_o}$ due to the noise. This is added as the time-dependent perturbative term,

$$H(t) = \frac{p^2}{2m_{Cs}} + \frac{1}{2} m_{Cs} \omega_{tr}^2 x^2 + \frac{1}{2} \epsilon(t) m_{Cs} \omega_{tr}^2 x^2 \quad (1.16)$$

The average rate at which a Caesium atom transitions from a state $|n\rangle$ to $|m\rangle$ in a time interval T is,

$$R_{m\leftarrow n} \equiv \frac{1}{T} \left| \frac{-i}{\hbar} \int_0^T dt' \frac{1}{2} \epsilon(t') m_{Cs} \omega_{tr}^2 x^2 e^{i\omega_{mn}t'} \right|^2 \quad (1.17)$$

We assume the averaging time is short compared to the time over which the populations in the levels vary but large in comparison with the correlation time of the fluctuations, allowing the extension of the range of integration to $\pm\infty$. Then, using the transition matrix elements ($m \neq n$) of x^2 and $\omega_{n\pm 2, n} = \pm\omega_{tr}$, the transition rates are given by

$$R_{n\pm 2\leftarrow n} = \frac{\pi\omega_{tr}^2}{16} S_\epsilon(2\omega_{tr}) (n+1 \pm 1)(n \pm 1) \quad (1.18)$$

$S_\epsilon(\omega)$ is the one-sided power spectrum of the fractional intensity noise written from its autocorrelation using the Wiener-Khintchin theorem. The power spectrum more specifically goes with the second harmonic of the trap frequency, indicating that we have a parametric heating process whose average rate is,

$$\begin{aligned} \langle \dot{E} \rangle &= \sum_n P(n, t) 2\hbar\omega_{tr} (R_{n+2\leftarrow n} - R_{n-2\leftarrow n}) \\ &= \frac{\pi}{2} \omega_{tr}^2 S_\epsilon(2\omega_{tr}) \langle E \rangle \end{aligned} \quad (1.19)$$

where $P(n, t)$ is the probability that the atom will occupy $|n\rangle$ at time t , the average energy is just $\langle E \rangle = \langle E(t) \rangle = \sum_n P(n, t)(n+1/2) \hbar\omega_{tr}$. This average energy increases exponentially,

$$\langle \dot{E} \rangle = \Gamma_\epsilon E \quad (1.20)$$

The rate constant $\Gamma_\epsilon \equiv T_I^{-1}(\text{sec}) = \pi^2 \nu_{tr}^2 S_\epsilon(2\nu_{tr})$ is written in terms of ν_{tr} which is the trap oscillation frequency in hertz and T_I is the time in seconds it takes for E to increase by a factor e called the energy e -folding time. The measurement of the power spectrum is then all that is required to know the heating rate given a certain noise performance of the laser in use for a particular trap frequency that scales as \sqrt{P} for a power P of the light ².

The raw laser noise can be effectively reduced by fine-tuning the laser and further suppressing it with a suitable system of opto-electronics. This has been installed previously and put to use in the 2-D experiment [46, 47]. For this reason, this thesis will report the laser intensity noise but will not cover its stabilisation and primarily focus on the other kind of laser noise, the one in its frequency.

² It has to be noted that for higher dimensional confinement, like in two dimensions in the 2-D lattice the form of the power spectrum is complicated by the fact that there are two trap frequencies (ν_1, ν_2)

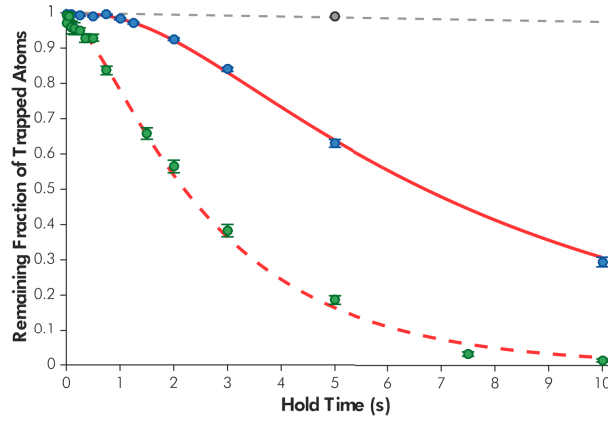


Figure 1.7: Intensity and Phase (Frequency) noise induced heating leads to a loss of atoms from the trap over time that can be numerically modelled with the Fokker-Planck equation. The influence of phase noise is especially on display here (intensity noise plays a smaller role that is not visible here) leading to a smaller storage time of 2.2s when it is high (extracted from the green data points with the dashed-line fit) than the case when the noise is relatively lower (blue data points with the solid-line fit) giving a storage time of 6.6s. The noise was exaggerated by adding electronic phase noise to the drivers of the AOMs in the experiment. The dashed grey line is the survival of the atoms purely limited by background gas collisions for comparison. (Image adapted from Robens [48]).

Frequency Noise

This is related to fluctuations of the laser light’s optical frequency and is interchangeably referred to as its phase noise. The oscillating light field of the laser either of a single frequency or one of multiple frequencies it could be operating in can vary in its optical phase in a manner that could be a random walk, a systematic drift or some combination of noise. The noise profile is known to fix the linewidth of the laser which is the width of the main peak in the power spectrum, usually at above the Schawlow-Townes limit if it is not completely white. This means the output of even a single-frequency laser is not a delta function centered at one frequency but spread out across a range of frequencies. Laser line-widths are therefore a measure of the degree of phase noise with narrow line-width lasers being preferred for exactly this reason that they have a low phase noise and so would have high spectral purity. To achieve as low a noise in this respect would be ideal for the experiment that insists on having light of precise frequencies and is sensitive to fluctuation.

Additionally, this noise manifests in another form in this experiment. Switching to an interferometric picture, the two counter-propagating beams generating the lattice along one dimension can be thought of as two arms of a Mach-Zehnder interferometer. If there is

and the intensity fluctuates possibly differently in each of them (see *Supplementary material* in [45]). Assuming the noise processes to be independent and the intensity fluctuations to be ϵ_1 and ϵ_2 in each trap frequency, the power spectrum is found to be

$$S_\epsilon(2\nu) = r^2 S_{\epsilon_1}(2\nu) + (1-r)^2 S_{\epsilon_2}(2\nu)$$

where $r = \nu_1^2 / (\nu_1^2 + \nu_2^2)$ is the trap frequency asymmetry parameter. The general argument and conclusion presented in the section above though still holds and serves to highlight the the need to quantify intensity noise.

a mismatch in the length of the arms of the interferometer and the frequency of the light is varying, there is an ensuing shift in the interference pattern. In other words, frequency fluctuations cause displacement of lattice position for an imbalance in the optical path lengths of the beams of the lattice. This is expressed as a phase shift $\delta\phi$ of the lattice given a non-zero path difference δL and a variation in frequency $\delta\nu$,

$$\delta\phi = \delta L \frac{2\pi}{c} \delta\nu \quad (1.21)$$

That translates in to a change in the average position δx of the lattice,

$$\delta x = \frac{\delta\phi}{2\pi} \frac{\lambda}{2} \quad (1.22)$$

written knowing that a phase shift of 2π is shift by $\lambda/2$ from one lattice site to the next (To distinguish the phase shift of the lattice referred to here from the intrinsic phase noise of the laser, the latter will be exclusively referred to as frequency noise from here on).

Frequency noise of the laser is hence a significant source of common-mode noise in the experiment which in the range of the trapping frequency would mean motional excitation of the trapped atoms and their eventual loss (Figure 1.7) because of the position jitter of the lattice. The heating rate of the atoms can be arrived at by a procedure similar to the one used before, modelling it as a perturbation of the trap center x_o ,

$$H = \frac{p^2}{2m_{Cs}} + \frac{1}{2} m_{Cs} \omega_{tr}^2 (x - (x_o + \delta x))^2 \quad (1.23)$$

Giving the heating rate,

$$\langle \dot{E} \rangle = \frac{\pi}{2} m_{Cs} \omega_{tr}^4 S_x(\omega_{tr}) \quad (1.24)$$

where $S_x(\omega_{tr})$ is the one-sided power spectrum of position fluctuations³. Here there is no exponential heating and it is independent of the average energy of the atoms. Scaling with the fourth power of the trapping frequency, it becomes large for deep traps used in the experiment. It becomes imperative, therefore, that we characterize the frequency noise of the laser used for the lattice. The dominating noise influence is mainly again from technical sources such as from the nature of the function of the laser's internal components. External vibrations and thermal drifts can also influence the frequency noise in the absence of good damping. It should be noted that there is also position jitter of the lattice caused by the use of AOMs for the polarisation synthesis in the DTQW experiments. This constitutes differential phase noise added on top of the laser frequency noise and has been measured earlier for the 2-D experiment [32].

But it is not enough that we measure the frequency noise of the lasers, since as discussed, they are made much more appreciable by the finite path length differences. In addition therefore, we need to measure the path lengths to quantify the full reach of their effect. In orders of magnitude, the position jitter is in the order of 10^{-12} m, calculated by

³ Similar to that of intensity noise, the power spectrum for position fluctuations will have a more involved form for a 2-D lattice accounting for the extra trap frequency.

substituting for a phase shift of 10^5 rad assuming an optical path difference of 10^{-2} m between the two counter-propagating arms in eqs. 1.21 and 1.22. In the best case scenario, we can expect the jitter to be restricted to only a few ångströms, limited by other effects such as the action of the AOMs [32]. The wavelength being in the order of a micrometre, this corresponds to a $\lambda/10^4$ stability of the lattice for which the optical path differences should be less than 1 metre. The path lengths will have to be measured to determine if they meet this requirement and adjusted if they do not, with the goal of reducing them to less than a metre.

OVERVIEW

The objective of achieving quantum walks on a lattice requires precise engineering of the techniques and instrumentation used, particularly in terms of their stability and versatility. The 2-D quantum walks experiment recently upgraded its laser source to two Titanium-sapphire (Ti:Sa) lasers that each output upwards of 5 W. Currently, one is in use for the MOT while the other, for the lattice. The high power of the new laser when used for the lattice ensures a potential depth of approximately 1 mK that prevents thermally induced hopping between lattice sites. The same power can also be homogeneously distributed over a large volume. This promises better homogeneity of the trapping potential which is needed for performing the atom interferometer or quantum walks. It also becomes possible to achieve coherence times of at least 10 ms. Integrating the laser into the experiment to achieve these coherence times and ensuring high stability during experimental sequences involves establishing whether the existing setup can accommodate the devices, supplementing them with further upgrades or additions if necessary. Analog and digital feedback control of laser power and careful, high precision polarization synthesis involving an optical phase locked loop have hitherto worked towards mitigating the intensity fluctuations and polarization instability of the laser light reaching the atoms. But, there still remains the question of the inherent frequency noise of the lasers and its suppression by ensuring the equalization of path lengths. For this, we begin with a general characterisation of the lasers.

2 | TI:SA LASER SYSTEM

The lasers to be evaluated are two Titanium:Sapphire (Ti:Sa) lasers, the *Matisse CS* and *Matisse CR*¹. The *Matisse CR* with an internal electro-optical modulator (EOM) has been set up for the MOT and the *Matisse CS* with an internal reference cavity set up for the lattice. The power output offered by the lasers at the set frequency is crucial for achieving optimum trap depth as is their promised single-mode operation, linewidth, noise performance and lock stability. In lieu of these requirements, this chapter will detail the efforts to set-up, measure and optimise them after first a brief description of the device, its internal elements and general function.

2.1 HARDWARE IN USE

Lasing in principle is achieved by having a gain medium that is pumped by an adequate source of light that is then amplified by the medium through feedback by an optical resonator. The self-exciting fields are endowed with special properties like high spatial coherence - they have a very small spot-size that comes close to an idealised light ray with a Gaussian transverse intensity profile (for the fundamental laser mode). It also has high temporal coherence - it has a limited spread in the frequency domain. The laser's single-mode operation is conditioned on the necessity that one of the resonator eigen-modes coincides with the center-frequency of the gain medium and the bandwidth of the medium is small relative to the free spectral range (FSR) of the resonator which is the difference in frequencies of its discrete modes. It is rarely the case though that the exiting light fields are of a single frequency. They instead possess a spread, the extent of which depends on the gain medium in use. In case of the Ti:Sa lasers where the medium is the Ti:Sa crystal which covers a specified wavelength range of over 1000 nm (300 GHz), this large a gain bandwidth would mean a vast number of modes can oscillate for any practical length of the resonator. To limit this spread in the frequency, additional frequency-selective elements need to be introduced into the resonator. The *Matisse* lasers have such elements for this very purpose arranged to have a loop geometry forming a ring resonator to aid amplification -

Birefringent filter: This element exploits the effect of birefringence to narrow the range of frequencies in which the lasing modes can exist. It consists of a stack of quartz plates oriented at the Brewster angle to let through light that is only p -polarised which sees no reflection off the plates at this angle whereas the s -polarised light will encounter high losses due to the reflection. The p -polarised light which enters the arrangement, then is split into the ordinary and extraordinary ray due to birefringence of the positive uniaxial crystal that is quartz. The two rays grow out of phase due to having different phase velocities through the plates, changing the polarisation of the beam. For certain

¹ both manufactured by Sirah

wavelengths the phase will be retarded by exactly one wavelength leaving the polarisation state unchanged. So for a given orientation of the optical axis which can be tuned by means of a stepper motor attached to the mount of the plates, only a certain number of wavelengths will see no change in their polarisation and will propagate out of the filter while the other wavelengths are reflected away. This element narrows the effective frequency range to approximately 50 GHz which is still a broad range to sift through which calls for ancillary elements.

Thin Etalon: A low finesse, solid state Fabry-Perót etalon of a fixed length with an FSR of 250 GHz, this element acts as another bandpass filter. It has a motor-controlled mount that allows control of the horizontal tilt of the angle of the etalon. This can be used to pick one of the etalon modes which has to be the same as the laser ring resonator modes. To ensure this, the reflection from one of the facets of the etalon is monitored and has a control loop associated with to adjust the etalon position in order to keep the ratio of the intensity of this reflection with the total laser intensity is kept constant. The frequency range is chosen by picking between the etalon modes with further filtering coming from the next element.

Piezo Etalon: This is another Fabry-Perót etalon but with FSR of 20 GHz. It is made of two prisms whose parallel bases face each other with a small air gap with one prism mounted on a piezoelectric actuator to control the thickness of this gap. Using the lock-in technique which involves dithering the piezo here at the frequency of 1 kHz, the center frequency of longitudinal mode of the etalon is maintained at the frequency of the laser resonator mode by monitoring the output of the etalon where the intensity variation is a translation of the frequency change. The cases of the etalon being either in or out of alignment would result in two distinct signals - one which corresponds to a scanning across the peak of the etalon mode giving a symmetric feature in the shape of a double U and the other being an asymmetric feature characteristic of sitting on the slope of the mode. The control loop seeks to hold the etalon at the position which gives the symmetric signal for that is where the etalon mode matches the laser resonator mode. This further narrows down the frequency range of the output of the thin etalon.

Woofers and Tweeters: The Woofer is also referred to as the slow piezo since it is a piezo-mounted tuning mirror that has an affiliated low-bandwidth control loop. It is used to control the length of the laser ring resonator and therefore also plays a role in determining the resonant modes. The Tweeter also works to change the optical path length of the beam in the cavity but is used for correction in the mid-range frequencies and so is also called the fast piezo. In device models which allow for an optional low-finesse reference cavity to go with the rest of the elements, the Tweeter works with the Woofer to counteract fast perturbations when locking to a mode of the reference resonator. The Woofer then behaves more like an auxiliary element - which is used to scan for the resonator modes prior to locking and post-locking, to keep the resonator at the center of its dynamical range to cancel out slow drifts of the laser in reference to the cavity. The two mirrors therefore help fix the frequency of the laser to a mode of the cavity using side-of-fringe or Pound-Drever-Hall locking methods, giving a fourth and final level of filtration of the emitted laser frequencies to guarantee its single-mode operation.

The laser also has a Faraday isolator made of a Terbium-Gallium-Garnet (TGG) crystal plate in a magnetic field that uses the Faraday effect to prevent two counter-propagating modes of the same frequency from co-existing in the laser which is made possible by its ring geometry. Reflecting between two mirrors and a partially transmitting optical element placed in a section of the path in the ring, a beam of the filtered frequency exits the device housing. This housing is isolated from acoustic vibration, has cooling pipes routed around some elements such as the Ti:Sa crystal to allow liquid coolant to flow and carry away any heat produced. The device also allow for complete purge of the internal atmosphere with Nitrogen gas to prevent the accumulation of dust, eliminate moisture and any organic deposits on the critical optics. The laser comes with a controller with the electronics necessary for driving the various piezos and implement the numerous control loops. The controller carries both analog and digital interfaces to manipulate the various elements. From amongst the analog inputs, one that goes through an on-board Digital Signal Processing (DSP) has proven particularly useful. The digital interface allows a personal computer (PC), which here is the lab computer that is the central control unit in the experiment, to connect to the controller and send commands over a serial port using either a provided graphical user interface (GUI) or using a user-defined software.

With locking to a specific frequency made possible by the above elements, the lasers are prepared by first ramping up the power of the Diode-Pumped Solid-State (DPSS) pump lasers (*Spectra-Physics Millennia eV*), lasing at 532 nm, up to a model-specific maximum of 25 W and re-adjusting its steering mirror that lies in its own, separate housing till the power readout of an integrated photodiode hits an optimum. The Ti:Sa lasers now being pumped are ready to be tuned and locked. The *Matisse CR* controller is fed with a Cesium spectroscopy signal through the one DSP input. The signal is obtained in the first place by using the light from the *CR*. The listed elements are used sequentially starting from the Birefringent filter to the woofer/slow piezo to narrow down the frequencies to the range which excites the various transitions of Cesium. A built-in Analog-to-Digital-Converter (ADC) digitises the signal and is available for live viewing in the GUI that then allows us to set the lock-point and subsequently lock the laser. Since the *CR* is to be used for the MOT, its frequency must be set for the "cooling" transition of Cesium which is the D₂ line. The spectroscopy signal has distinct features corresponding to the various transitions with the one associated with the $|F = 4\rangle \rightarrow |F' = 5\rangle$ transition being chosen for locking this laser at the frequency which is around 351.72188 THz. The *Matisse CS* - a model that comes with the optional reference cavity with side-of-fringe locking - is tuned to output light at the "magic" wavelength of 865.8 nm, or more precisely in frequency,

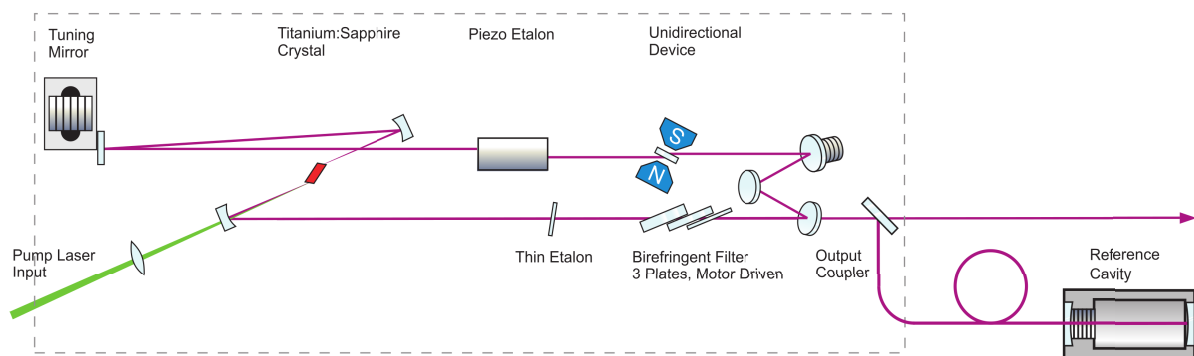


Figure 2.1: Schematic of the *Matisse CS*

346.18916 THz using the readout of a *High Finesse* wavemeter and is utilised as the source for the lattice beams.

2.2 LASER INTENSITY NOISE

Having learnt of the laser function and locked the laser to the desired frequency, the obvious next step was its characterisation starting with the intensity noise. The fluctuations of the laser power $\delta P(t)$ are usually quantified *relative* to the average power $\langle P \rangle$ called the Relative Intensity Noise (RIN). Conventionally, the RIN^2 is reported which is exactly defined as the ratio of the mean square optical intensity deviation in a 1 Hz frequency bandwidth at a specified frequency and average optical power to the square of the average optical power,

$$\text{RIN}^2 (1/\text{Hz}) = \frac{\langle \delta P^2 \rangle}{\langle P \rangle^2} \quad (2.1)$$

The intensity fluctuations are measured along a range of frequencies with the resulting one-sided power spectral density normalised by the average power given by,

$$S_I(\nu) = \frac{2}{\langle P \rangle^2} \int_{-\infty}^{+\infty} \langle \delta P(t) \delta P(t + \tau) \rangle \exp(i2\pi\nu\tau) d\tau \quad (2.2)$$

This is the sought after power spectral density of RIN but it does not include what is likely to be measured since that would be an overall noise with two more components over the pure laser intensity noise which is the thermal (electronic) noise and shot noise that need to be subtracted away for a precise estimate of the RIN. The measurement of this overall noise of the *Matisse* lasers was carried out when they were first installed using a Network Analyser (*Agilent/HP 3589A*, Range: 10 Hz to 150 MHz at 1 M Ω input impedance), analysing the DC signal from a photodetector (*Thorlabs PDA10A-EC*, Bandwidth: 150 MHz) placed as close as possible to the output of the laser with no intervening optics and the pump lasers at their full power of 25 W. The spectrum obtained of one of the lasers ([Figure 2.2](#)), showed peaks at 50 Hz and its harmonics which is noise from the power-line. There was a small and wide peak at around 1 kHz, the first indication of noise contribution due to the function of the device itself since we know one of the internal elements, the piezo etalon, is active at this frequency. It had a more prominent peak at 2 kHz which could be the transient relaxation oscillation caused by a change in the pump power which are usually found in the kHz regime. Several smaller peaks were also to be found in the 10 kHz to 1 MHz range which could be either due to action of the internal components or completely spurious. Regardless of the exact origins of the various peaks, comparing this RIN spectrum which is of the *Matisse CS* used for the lattice to that of the previous laser in use (the *Coherent MBR*), we see the noise level is two orders of magnitude smaller in the entire range of frequencies up to 100 kHz beyond which we see the roll-off to the shot noise limit. This inference is backed by the values acquired by integrating the RIN in a certain frequency range called the integrated RIN which for the *Matisse CS* was 0.106% (10 Hz - 1 MHz) to the 0.226% (10 Hz - 1 MHz) of the *Coherent MBR*. With this marked improvement already, the analog and digital

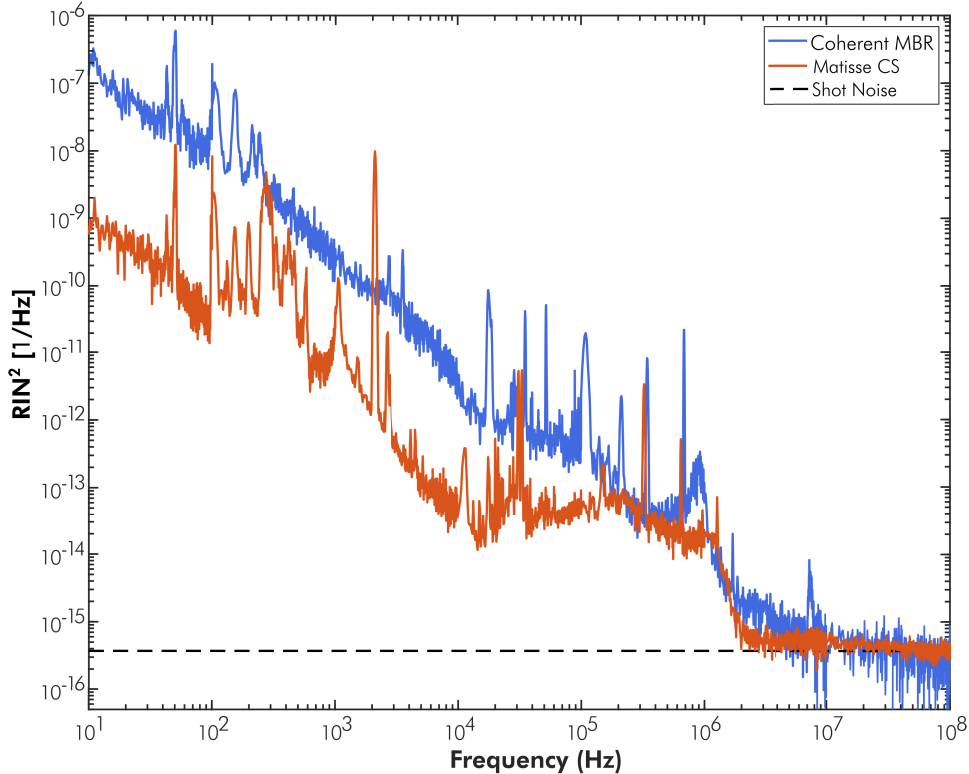


Figure 2.2: The RIN power spectral density, containing also the background thermal/electric noise and the shot noise, as measured for the old *Coherent MBR* and its replacement the *Matisse CS* for use as the source for the lattice beams.

intensity stabilisation control loops that are in place downstream in the experiment are less stressed and with recent enhancements [47], can potentially provide an unprecedented noise floor for the experiment.

A caveat must be included here - this RIN was measured early in the life of the *Matisse CS* and its pump laser. Over the duration of a year, the system performance noticeably changed with the laser degrading in terms of its noise performance. A regular high frequency noise feature was noticed when a photodiode signal was monitored on an oscilloscope. The reason was traced back to the *Millenia* pump laser in use after their RMS power was logged for a period of time. Consistent excursions from a more acceptable RMS of 0.01% to one in excess of 0.2% were noticed that did not improve with suggested optimisation protocols but did reduce only when the operating power was reduced from 25 W to 22 W. Since this was not ideal, the pump laser was subsequently exchanged along with the pump laser for the *Matisse CR* (MOT) laser which also was learnt to possess a technical glitch. It remains to be seen if the issue has been resolved.

2.3 INTENSITY NOISE IN OPTICAL FIBRES

Beyond the intensity noise of the lasers themselves, another form of intensity noise presents itself when tasked with the handling of the high powers (in excess of 5 W) that are now available. Light from the lasers needs to be transported via fibres from the laser to the experiment ensuring that it is in a single mode, usually the TEM₀₀ mode, which allows the focusing of laser beams onto the atoms at the diffraction limit

while also maintaining the polarization purity. This is presently done with a conventional single-mode, polarisation maintaining step-index fibre in the experiment into which light with powers up to 1 W is coupled in. Transporting power of more than 1 W however brings with it technical challenges like the effect of Stimulated Brillouin Scattering (SBS) because of their small mode field diameter which results in large intensity noise that can heat out atoms from the trap. The extent to which this plays a role was previously determined for this experiment. Brillouin scattering is a third-order non-linear process involving an inelastic collision between a photon and a phonon generated in the fibre by electrostriction by the same photons. An incoming photon is back-scattered off the phonon, being also shifted in frequency. The effect grows non-linearly and is stronger for higher optical powers when it can become a stimulated process with the phonon population increasing substantially. Above a certain threshold power, the now Stimulated Brillouin Scattering reflects back most of the coupled light. This power has a particular dependence on the effective mode area A and length L of the fibre as given by the approximation [49],

$$P_T \propto \frac{A}{L} \quad (2.3)$$

The maximum power that can be sent into the fibres consequently grows with the mode area of the fibres but falls with its length. The fibres in use in the lab have a mode area of $5.3 \pm 1.0 \mu\text{m}^2$ and are 10 ± 0.075 meter in length as they need to be drawn between two

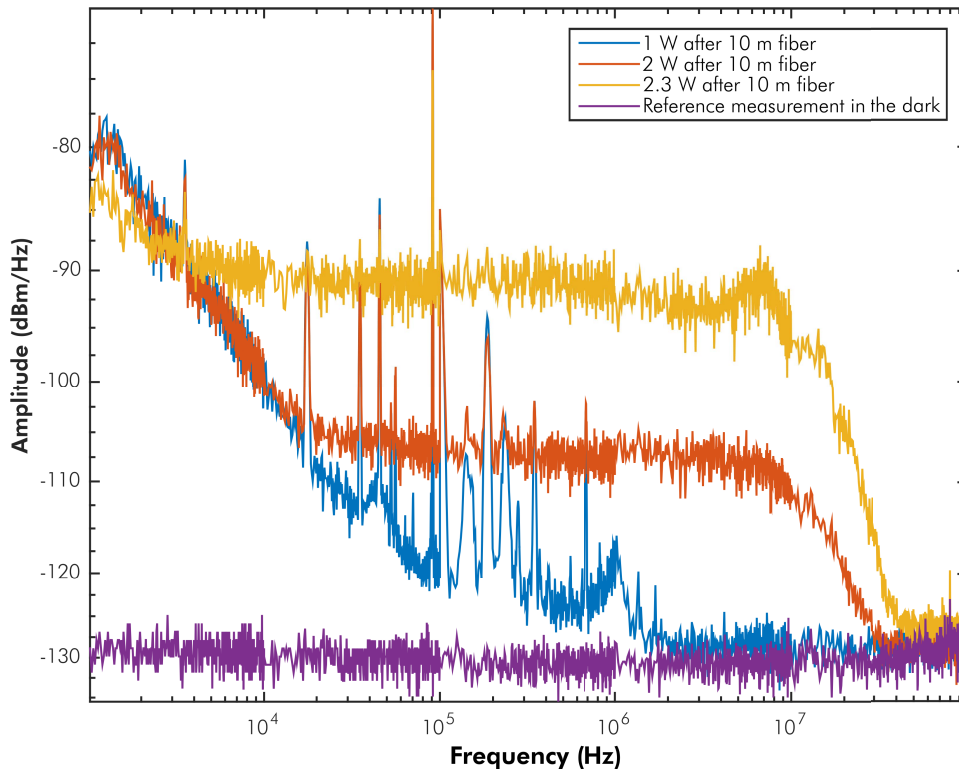


Figure 2.3: Intensity noise power spectral density as measured at the end of a 10 m optical step-index fibre for light of increasing powers starting from 1 W. The noise was found to increase for the higher powers for long fibre lengths ((10m) but limited for the same powers being coupled into fibres of same mode area but shorter length (1m). The damage threshold of these fibres is also a significant limiting factor.

optical tables. Coupling light into one of the fibres at first 1 W, then 2 W before finally 2.3 W and measuring the noise at the other end of the fibre every time, it was found the SBS was very pronounced, the noise level rising with the larger powers (Figure 2.3). To circumvent this, the powers coupled into the fibres have so far been limited to 1 W with the experiment left wanting elevated powers for deeper traps. In order to transfer $> 2W$ of light from the *Matisse* laser for the lattice along with the $> 20W$ of laser light from a 1064 nm *Mephisto MOPA* laser that is used for the vertical dipole trap that is present for vertical confinement of the atoms in the horizontal lattice, an upgrade from the step-index fibres with small mode area to large mode area fibres was regarded as necessary which should reduce the effect even if the length of the fibres is left the same for practical reasons. On that account, a switch to endlessly single mode, polarization-maintaining photonic crystal fibre was decided upon.

2.3.1 Photonic Crystal fibres

Photonic crystal fibres (PCFs) [50] consists of a solid/hollow fibre core and a regular arrangement of microscopic, wavelength-scale, air-filled holes that run through the length of the fibre cladding allowing for low-loss guidance of light through the core, a structure similar to that found in photonic crystal - hence the name. This gives it numerous novel properties like endless single mode operation, high degree of nonlinearity, controllable birefringence and dispersion characteristics. More relevant to the current application, these fibres will also have a higher SBS threshold and a higher laser damage threshold both of which are 4 times higher because of the fact that the PCFs have a mode field diameter which is 2 times larger (both thresholds are linearly proportional to the effective area calculated from the mode field diameter) than the regular step-index fibres.

It was realised early on that only bare PCFs can be bought off the shelf unlike the angle cleaved, AR-coated, fully connectorised patch cables made of the regular step-index fibres. These bare PCFs have to be prepared for use. The PCF first has to have its holes collapsed at the end facets. The resulting larger core diameter reduces end face power density and reduces power density related effects. It also reduces Fresnel back reflection coupling efficiency and hermetically seals the Photonic Crystal fibre preventing any contamination. Then at the now solid end facet, the fibre needs to be cleaved with an angle which is large enough to absolutely make sure that there is no back reflection that couples into the fibre. Anti-Reflection (AR) coating is also required covering the wavelength range around the operating wavelength to further ensure that there is no back reflection. In the end, the fibre needs to be jacketed and connectorised with preferably a connector that can withstand high powers.

After initial in-house attempts at hole collapse of a small length of PCF using the available splicer and cleaver was found to give mixed results, industrial expertise was sought to ensure consistent, reliable quality of the end result. A seller was found from whom an offer for custom patch cables of PCF prepared with the required specifications is being procured. The fibres acquired in this manner will have end-caps instead of collapsed microstructure, SMA connectors for angle-cleaved fibres and AR coating, which otherwise was not offered as a service by other sellers. Custom collimators are also being sought. With this complete set of custom fibres and collimators, the installation can be carried out with minimal effort.

2.4 LASER FREQUENCY NOISE

Having addressed intensity noise in its two forms, the next examination is that of the laser frequency noise. For the determination of this noise, a device and a measurement schema to go with it becomes necessary. Frequency noise estimation by direct optical measurement is done in predominantly two ways - Homodyne detection where a beat note with a second low-noise source or with the same source with added delay is created and analysed; Using an optical frequency discriminator like an scanning optical resonator to convert frequency modulation to intensity modulation. The latter is to do with the transmission in an optical resonator which, due to the nature of the resonator's operation, is a result of the decomposition of the input into its spectral components and visible as a time series of modulated intensity with distinct, characteristic peaks corresponding to resonant frequencies. Sitting on a point slope of one of the peaks where it is most sensitive, an optical resonator will convert the source frequency fluctuations into amplitude fluctuations in the two directions about the point. Called side-of-fringe locking in an optical resonator, this is convenient and relatively easier to implement to the homodyne method but has trade-offs: High frequency resolution is difficult to achieve, it has a low signal to noise ratio, low stability and it can be difficult to differentiate between frequency and actual intensity fluctuations. Another drawback is the active lock to a point on the slope necessary for the proper operation of the resonator as a discriminator - the range of frequencies over which the measured frequency noise is valid is limited to above the servo bandwidth of the lock. We show here that, despite these shortcomings, a reasonable estimate of the laser frequency noise can be obtained using this approach with a few considerations.

2.4.1 Optical resonators

Optical resonators or optical cavities are a construction of mirrors that reflect light between them to form a standing wave of light for certain resonant frequencies which are transmitted through the mirrors showing a spectrum that typically consists of closely-spaced peaks with a certain linewidth. The distinguishing features of the various types of resonators that exist are the radii of curvature of the mirrors used and the distance between them. The configurations are usually chosen based on the type of application which demand one or a combination of criteria be met. These criteria include stability, Q-factor and ease of alignment among others.

The simplest resonator to consider is one formed of two opposing mirrors, called a Fabry-Perot cavity. Suppose one such cavity was made of two mirrors, each with a radius of curvature R_1 and R_2 , having high reflectances ($r_{1,2}$), low losses ($a_{1,2}$) and being partially transmitting ($t_{1,2}$). The mirrors are placed with their reflecting surfaces facing each other and separated by a length L . Light waves which can enter the cavity through one of the mirrors undergo sustained reflections between the mirrors. During the multiple round-trips, the waves constructively interfere which leads to a building up of an intracavity field that is transmitted provided the phase-matching condition is met which is that an integer multiple of half the wavelength should fit within the length of the cavity: $n\frac{\lambda}{2} = L$. All other wavelengths destructively interfere. More generally, the wavelengths, or equivalently, the frequencies which will be supported in the cavity can be

analytically derived by solving the paraxial wave equation for a Gaussian beam and is given by,

$$\nu_{qmn} = \frac{c}{2L} \left[q + \frac{1}{\pi} (m + n + 1) \cos^{-1} \sqrt{g_1 g_2} \right] \quad (2.4)$$

here c is the speed of light while q, m, n are numbers which distinguish the various Hermite-Gaussian or the Gaussian transverse electromagnetic (TEM) eigen-modes of the cavity whose associated frequencies are given by the expression above. g_1 and g_2 are the g -parameters of each mirror given by $g_{1,2} = 1 - L/R_{1,2}$ which define the stability for the numerous geometries of cavities as is made possible by the choice available of mirrors of different radii of curvature and the distance of their separation. The condition for this stability is $0 \leq g_1 g_2 \leq 1$ which needs to be fulfilled for the periodic re-focussing of the intracavity beam which can otherwise grow limitlessly and be lost.

So an arbitrary (quasi-)monochromatic light field entering a stable cavity is decomposed into a number of TEM _{qmn} cavity modes. The TEM _{$q00$} , called the fundamental longitudinal (or axial) mode, can be resonant along with the higher-order TEM _{qmn} modes for $m, n > 0$ for the particular mirror separation with the full bandwidth of possible resonances revealed when the cavity length is scanned, as is typically done. Of the many combinations, the spherical mirror or confocal Fabry-Perót cavity is most suited for general application. The reason for this being the loose tolerance on the proper beam alignment required (traded for a tight tolerance on mirror separation) to obtain the transmission spectrum of mostly only longitudinal modes, unambiguously spaced far apart with high transmission. This is made possible due to the mode degeneracy. A spherical mirror Fabry-Perót cavity is comprised of two identical spherical mirrors separated by a distance very nearly equal to their common radius of curvature. This would mean the mirrors have the same radius of curvature, $R_1 = R_2 = R = L$. It follows that the g -parameters are zero, so eq. 2.4 reduces to,

$$\nu_{qmn, \text{Conf}} = \frac{c}{2L} \left[q + \frac{1}{2} (m + n + 1) \right] \quad (2.5)$$

It is immediately apparent that several higher order TEM _{qmn} modes share the same frequency as the fundamental TEM _{$q00$} (more precisely, all the even-symmetry transverse modes of the cavity are exactly degenerate at the longitudinal mode frequencies of the laser). The spectrum will have a regular, equidistant mode structure with the spacing between two consecutive modes called the cavity's (confocal) Free Spectral Range (FSR),

$$\nu_{\text{FSR, Conf}} = \frac{c}{4L} \quad (2.6)$$

which is half the spacing that will be otherwise seen if the incident light is spatially mode matched to the fundamental TEM _{$q00$} mode, that is, when the wavefronts of the Gaussian beam perfectly match with the mirror surfaces and the incoming beam is aligned to the optical axis of the resonator. In that case, no higher-order modes are excited with only longitudinal modes visible, spaced $c/2L$ apart. The mode-matching however is not always perfect giving rise to higher-order modes, also called half-axial modes (which are all the degenerate odd-symmetry transverse modes), midway between the longitudinal modes

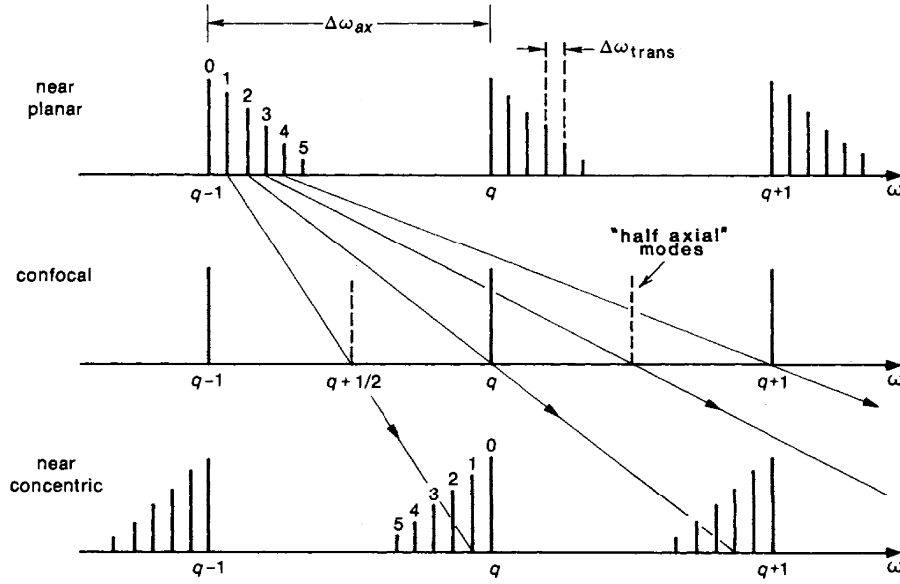


Figure 2.4: Resonant mode frequencies in various stable (Gaussian) resonator configurations. The frequencies are represented by ω with $\Delta\omega_{ax}$ being the longitudinal/axial mode spacing and $\Delta\omega_{trans}$ is the transverse mode spacing. In our desired confocal configuration, all even-numbered modes are degenerate with the axial modes while all odd-numbered modes are degenerate at the frequency halfway between consecutive axial modes as depicted here. Image taken from Siegman [51].

(Figure 2.4). Careful alignment and mode-matching with the right optics can suppress these modes, with an improvement in the maximum transmission along with the increase in the FSR.

The effective use of the cavity as a frequency discriminator to measure frequency noise would depend critically on how well the device can resolve and portray in its response the changes in frequency. To a large extent, this is limited by the reflectivity of the mirrors of the cavity that determine the full width at half-maximum (FWHM) of the modes in the spectrum which have a Lorentzian line shape. A low-reflectivity mirror would yield broad transmission peaks which would mean a reduced sensitivity to changes in frequency if we employ the side-of-fringe locking and sit on a point on what will be a slowly rising edge of the peak. A high-reflectivity mirror on the other hand will yield a narrower transmission peak and a steeply rising peak would make the device responsive to a greater degree, as would this mean a high spectral resolution in a wide spectral range. For cavities, this is usually indicated by a quantity called Finesse (or the Q-factor, which is the resonance frequency divided by the FWHM, but can be restated in terms of the finesse) which is defined as the ratio of the free spectral range to the FWHM or equivalently in terms of the reflectivity,

$$\mathcal{F}_{\text{Conf}} = \frac{\pi\sqrt{r}}{2(1-r)} \quad (2.7)$$

With this it becomes clear that a confocal Fabry-Perót cavity with good mode-matching and high Finesse would be desirable. To this effect, an assembled confocal Fabry-Perót cavity that was available for use in the lab was set up but - with a finesse of ~ 150 and peak transmission of $\sim 0.5\%$ - found to fail to meet these prerequisites meriting a rebuild.

2.4.2 Construction of a high finesse Fabry-Perót cavity

All of the designs and components required for this build were readily available as they were made, purchased or pre-fabricated for earlier attempts to build Fabry-Perót cavities in the lab by Dr. Jose Gallego. To re-assemble a new, high finesse confocal Fabry-Perót cavity however, a careful selection of the components was undertaken and caution shown during the build itself which was one of the other noticeable shortcomings of the available cavities many of which had unstable mounting and occluded or damaged optics. A stock of *MSPV12.5B/-50* plano-concave mirror substrates from *Lens-Optics* was found in the lab inventory. As per the manufacturer, the mirrors were made of BK7 glass with a radius of curvature of -50 mm, a diameter of 12.5 mm and a thickness of 6 mm. It is supposed to be highly reflecting between 780 – 1064 nm and has a high Laser Induced Damage Threshold (LIDT) of 40 W/mm. These specifications regarded them as ideal mirror surfaces for this application. The mirrors, stated to have a lower bound of $R > 99.5\%$ on the reflectance, were then each measured in terms of its transmission to find a pair of mirrors closest in their transmittance as part of impedance matching which is done to minimize losses via back reflections of the incident power. This strictly does not guarantee impedance matching since there are losses to consider for which then the impedance matching condition is that the transmittance of the input mirror must equal sum of the transmission of the other mirror and all the losses present. But since they were not stated by the manufacturer and are not easily determined, the losses were discounted and two mirrors both with a transmittance of 0.07% were found and chosen to be used for the cavity. At the moment of choosing, the possibility that the mirrors were of very high reflectance of nearly 99.9% outweighed the likelihood that the losses - a blend of absorptive and scattering losses - were very dominant.

The use of mirrors with radius of curvature of 50 mm meant that, for confocality, they must be spaced apart by 50 mm. Although the mirrors can be mounted on standard mirror mounts and aligned on the optical table in the open, since the length of the cavity is so critical and temperature, air currents are significant disturbances, only complete mechanical and thermal isolation will enhance the stability of the cavity. A machined Aluminium rod, 65 mm in length and 25 mm in diameter, was therefore taken to be used as a housing for the mirrors. The rods were designed to have insets into which plastic caps would be inserted and glued in place. At the input end, a flat cap was used that was notched on one side to hold a piezoelectric tube actuator on to the end of which one mirror would be glued using epoxy to enable the scanning of the length of the cavity. The piezo itself is a tube of monolithic ceramic that contracts axially and radially when voltage is applied across its metalised inner and outer surfaces. The particular piezo tube used here offered by *Piezomechanik GmbH* was 36 mm long, had a diameter of 10 mm and thickness of 1 mm. It had a stated axial contraction of 16 μm with only 3 μm radial contraction (this needed to be kept to a minimum as a radial movement would be undesirable) and a specified maximum voltage range of -200 to 1000 V. The assembly of cap with the piezo tube and one of the mirrors was then pushed into place with the mirror position being inside the Aluminium rod. For the other output end, the second mirror was first inserted into a hollow M16 brass rod that was specially designed by the institute mechanical workshop to be threaded on both the inner (pitch of 1) and outer surfaces (pitch of 0.5) of the rod. The rod was 26 mm in length and had a 3 mm strip of metal extending out from the inner surface against which the mirror was held in place with a

rubber spacer that could be threaded in. This was followed by a collecting lens *LA1560-B* which is a plano-convex spherical singlet lens also held in place by a spacer, made of N-BK7 glass with a diameter of 12.7 mm and focal length of 25 mm. The brass rod with the optics inside was then turned into a second plastic cap that had a female thread to accommodate the outer male threading of the brass rod. The cap was then slipped into place at the remaining end of the Aluminium rod. The rationale for the outer threading of the rod is the need for initial adjustment to ensure the mirror separation is 50 mm as required for the cavity to be confocal. Final adjustment needed to be done by coupling light into the cavity at the input. This was done in a test setup with a voltage ramp applied to the piezo and the brass rod rotated till the expected confocal mode structure was seen in the collected spectrum at the output at which point, the required mirror separation would have been reached. It was here that in following the best practices of aligning a Fabry-Perót cavity [52, 53] that the dominant nature of spherical aberration and its role in causing a deviation from the ideal, symmetrical Lorentzian line shape of the modes in the observed spectrum was learnt of.

Modified line shape due to spherical aberration

In accordance with paraxial optics, a ray of light which enters the spherical mirror cavity close to the axis joining the centers of the two mirrors, traverses a path that it is reflected back on to - the ray suffers a total of four reflections before it is re-entrant at the same initial point. Spherical aberration, however, prevents the ray from re-tracing its path. The sphericity of the mirrors refocuses a ray incident at each point on one mirror to a different set of points on the other mirror leading to a staggered set of paths taken by the ray over multiple reflections. For one transit between the mirrors involving four reflections, the paraxial path length for the ray, given the more general case of the spacing between the mirrors being slightly off confocal by ϵ , is given by $4(R + \epsilon)$. With spherical aberration, if the ray enters the cavity at a position that is offset from the axis by some distance ρ , this path length is less by an amount given up to leading order by,

$$\Delta(\rho) \sim \frac{\rho^4}{R^3} + \frac{4\epsilon\rho^2}{R^2} \quad (2.8)$$

which can be arrived at geometrically [52]. There is a multiple beam interference pattern that is formed in the central plane of the cavity subject to a modified phase matching condition for some integer m ,

$$4(R + \epsilon) - \frac{\rho^4}{R^3} - \frac{4\epsilon\rho^2}{R^2} = m\lambda \quad (2.9)$$

In a beam of a large enough diameter incident on the cavity, there will be multiple rays of light some of which will be on-axis while some will be off-axis. The whole input beam itself could be offset. In these cases, spherical aberration becomes significant. The result is that marginally different mirror spacings satisfy the phase matching condition and the measured line shape is broadened assymmetrically. This modified line shape is noticed as a peak with a leading or lagging tail. The total instrumental finesse now is no longer just determined by the reflectivity of the mirrors and has an additional term called the illumination finesse (there is also a third term that accounts for a symmetric broadening of

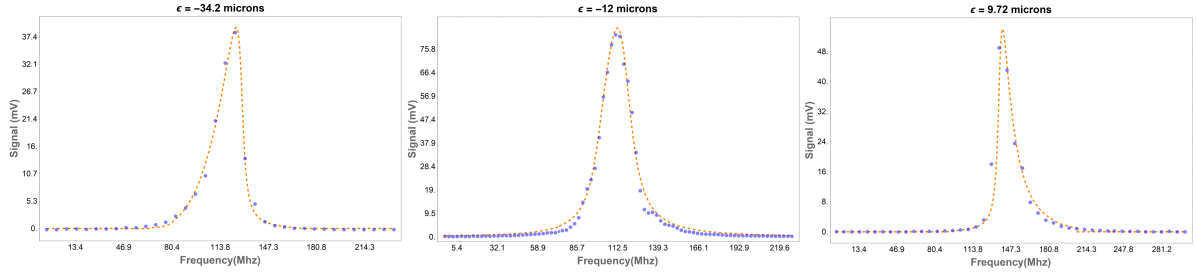


Figure 2.5: The traces of the cavity signal (data points in purple) at different mirror spacings about the confocal setting, fit with the line shape (dashed orange line) that accounts for spherical aberration. A negative ϵ implies a mirror spacing shorter than confocal by the stated magnitude and a positive value implies a spacing longer than confocal.

the line shape due to mirror surface irregularities that cause random position-dependent path length difference that blurs the line shape. This though is pronounced only for mirrors of surface quality much poorer than the $\lambda/10$ specified for the mirrors used in our cavity),

$$\frac{1}{F_t} = \frac{1}{F_r} + \frac{1}{F_i} = \frac{2(1-r)}{\pi\sqrt{r}} + \frac{4\rho^4}{\lambda R^3} \quad (2.10)$$

This finesse changes negligibly for small beam diameters but decreases as the beam diameters increase with greater tolerance seen in confocal cavities with mirrors of a large radius of curvature and so a long length. For our re-assembled cavity, this threshold was 0.5 mm.

A theoretical model of the expected line shape in the presence of the aberration was drawn up as a more accurate function to fit the modes in the measured cavity spectrum, as would be especially needed to precisely calibrate the cavity for its use in the frequency noise measurement. This was done by convolving the ideal Lorentzian as the mirror spacing is being scanned by $\delta\epsilon$ with a Gaussian laser mode having an axial waist ω_o and radial extent ρ as solved for by using the phase matching condition,

$$I(\rho, \delta\epsilon) = \frac{1}{\sqrt{2\pi\omega_o^2}} e^{\frac{-2\rho^2}{\omega_o^2}} * \frac{1}{1 + \left(\frac{\delta\epsilon}{\text{FWHM}}\right)^2} \quad (2.11)$$

With this theoretical model, it was noticed that in the event of being limited by the spherical aberration, the confocal separation is not ideal if a narrow, tall and symmetric peak is desired for the modes in the cavity spectrum. Instead, the spacing should be slightly off confocal. this was backed by the measured line shapes obtained when positioning the second mirror to complete our cavity assembly. A collimated beam of an estimated diameter (radius) of 1.1 mm was coupled into the cavity to inflate the aberration during the task. Traces of the collected intensity profile for three cases - assymmetric line shape with a tail to the left, a symmetric line shape and assymmetric line shape with a tail to the right - where fit with the custom function with the deviation from the confocal mirror separation as one of its free parameters (Figure 2.5).

Identification of mode-matching optics

Having put together the cavity in the manner described, the final step was to improve alignment and transmission for which, in addition to lining up the laser beam along the optical axis, a suitable mode-matching optics was introduced. This was a single lens needed to focus down the beam to the center of the cavity to match the input Gaussian beam to the fundamental cavity mode. Going beyond simpler approaches like a ray-transfer matrix analysis, the choice of the lens was made by putting to use a new MATLAB-based ray tracing tool developed for the lab by Dr. Andrea Alberti. The tool allows the import of entire *Zemax* catalogues of optics available for download from various manufacturers to be used for design in other proprietary ray-tracing softwares like the *Zemax OpticStudio*. The catalogues are design files for every item in an exhaustive list of optics from simple lenses, aspheric lenses, gradient-index lenses to mirrors and diffractive optical elements. The files detail the form of the elements in terms of the focal lengths, radius of curvature, glass material and coating used in its construction and surface quality among others. This allows a drawing of the entire optical system of interest with each element is put together from surface to material to surface and simulate the propagation of rays through it. This particular tool was written to identify the right optical system to use for expanding the MOT beams in the experiment to trap a larger number of atoms and has proven useful in modelling optics in other projects since. Beyond mere simulation, the tool also provides analysis and optimisation options that report on the calibre of the system with useful measures like the phasefront quality and can improve them by readjusting spacing between the placed elements. While the tool is more expansive in its options, these two exclusively were exploited for the exercise of selecting a mode-matching lens for the cavity.

The entire cavity was first modelled by drawing its mirrors surface by surface as is also possible with the tool (Figure 2.6(a)). Simple lenses were then drawn up from the catalogues and placed in front of the cavity. The tool was then tasked to simulate the

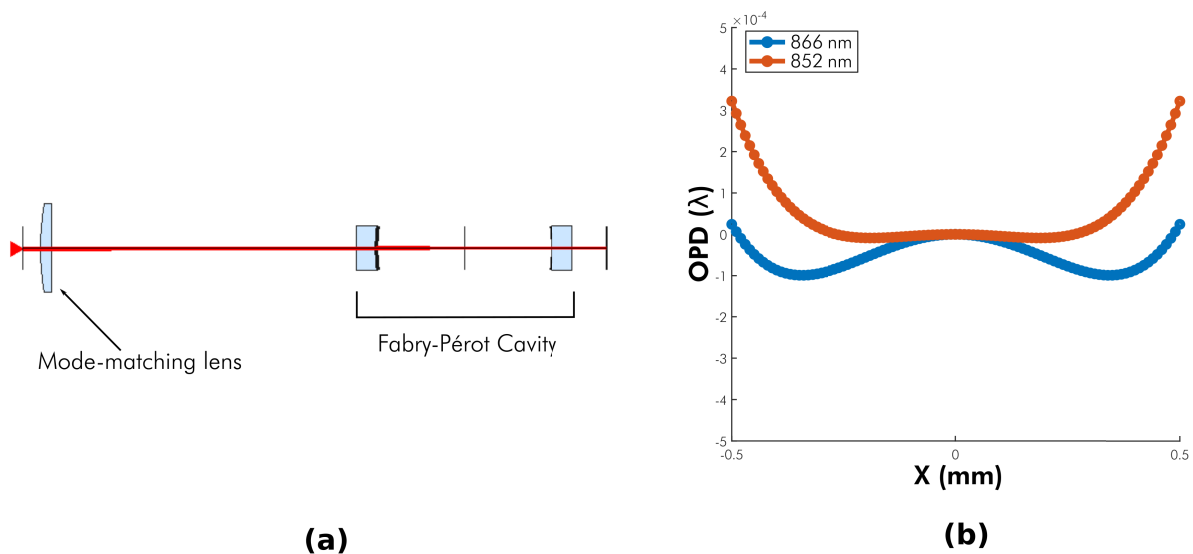


Figure 2.6: (a) The ray tracing tool provides convenient visualisation of the system being simulated like done here for the cavity with a mode matching lens. (b) The resulting phasefront quality with using the *LA1433-B* as the mode-matching lens for the two wavelengths of 866 nm and 852 nm.

system with slight modifications made to the code on how the cavity dynamics is handled. From a plano-convex lens of diameter 12.7 mm and focal length of 25 mm to another of 25.4 mm and 300 mm respectively, a total of 9 lenses were tried with some requiring manual optimisation to identify the right lens and spacing to use by noting the Strehl ratio and phasefront quality at a specified exit pupil. For its near uniform phasefront when 86.875 mm from the surface of incidence of the first mirror and additional pragmatic considerations, the *LA1433-B* plano-convex lens with a diameter of 25.4 mm and a focal length of 150 mm was decided on and used (Figure 2.6(b)).

Calibrating the cavity

Steering a collimated laser beam to the now completed cavity assembly and carrying beam walking to obtain the mode spectrum, the different modes were identified and the maximum transmission measured. Despite extensive beam walking and the mode-matching lens, the half-axial modes could not be extinguished although some reduction in their peak height could be achieved. The FSR so was still given by $c/4L$ and was 1.5 GHz. It was also found that the maximum transmission now was at 2%, a four-fold increase over the previous value but one that is markedly below other reported transmissions for mode-matched confocal cavities [52] of nearly 50%. This could be explained by the absorptive and scattering losses we earlier overlooked. The losses are perhaps not as miniscule and strongly limit the net transmission out of the cavity which given as [52],

$$T_o = \frac{1}{2} \left[1 + \frac{a}{t} \right]^{-2} \quad (2.12)$$

If a is the common sum of the absorptive and scattering losses and t , the common transmission through the mirror coatings, there is a drastic loss in the net transmission when the absorptive and scattering losses as a sum become comparable or exceed the transmission loss at the mirror. With losses that could be as high as 0.43% given the lower bound of 99.5% on the reflectivity and 0.07% measured transmission, this could very likely be the case. Large values of a/t often lead to a compromise between finesse and transmission but the finesse was yet to be determined given this transmission of 2%.

The cavity was first transferred to near the *Matisse* lasers on an optical table that is decoupled from its environment. A telescope consisting of lenses, put together to tighten any input beam down to 0.5 mm before being steered into the cavity, was added to the system. To estimate the total finesse and also determine since the conversion between the intensity fluctuations of the locked cavity signal and the frequency fluctuations of the laser needs to be known, a calibration of the cavity was required. Coupling in light from the lasers and scanning the length of the cavity would be one way to do this but this has a drawback which is that the displacement of the piezo element is subject to hysteresis [54]. Scanning of the piezo tube actuator therefore might not necessarily lead to a smooth linear behaviour all throughout. This can be seen as the varying width of the line profile between the successive modes as the voltage to the piezo is ramped. To circumvent this, it is common to scan the frequency of the laser and extract the trace of the line profile and fit a function like our custom function from eq. 2.11. This was possible with the scanning of the reference cell of the *Matisse CS* with which the finesse was determined to be 250, a nearly two-fold increase from the old value. The conversion factor was acquired by calculating of the slope at the half-way point of the peak, in its most linear region

which is where it is ideal to lock to. (The same was not done for the *Matisse CR* which, owing to the lack of the reference cell, could not be trivially scanned over a given range with the internal locks active as would be necessary to prevent mode-jumps. The right scan parameters for the only element for which the functionality was available in the *CR*, the woofer/slow piezo, needed to be determined which was not done in the interest of time. The conversion factor was obtained by the other method of scanning the length of the cavity which still would give a feasible value for the frequency noise of the *CR*. This was deemed acceptable considering it was the frequency noise of the *CS* that is arguably more important and demanded a more precise estimation).

2.4.3 Measurement of frequency noise

The newly built cavity was now set to fulfill its purpose of measuring the frequency noise which was done of both the *Matisse CS* and *Matisse CR* lasers with the setup shown in Figure 2.8. The cavity lock was achieved by a simple servo feedback loop. The output was collected by a photodetector (*Thorlabs PDA10A-EC* (Bandwidth: 150 MHz)), the signal from which was split in two with one carried to the network analyser (*Agilent/HP 3589A* (Range: 10 Hz to 150 MHz at 1 M Ω input impedance)) for the noise measurement and the other to the custom PI controller (*Lockbox 5*) as the error signal with the internal offset setting used to raise or lower the signal to have a zero-crossing at the desired lock point. The control signal from this box was then sent to the piezo of the cavity through a high voltage driver. Since the locking had to be limited to arrest only low frequency drifts, a second-order low pass filter was added with a corner frequency of ~ 100 Hz between the piezo driver and the cavity since while still being part of the control loop, it would also limit any high frequency noise components added to the signal by the driver. Using a

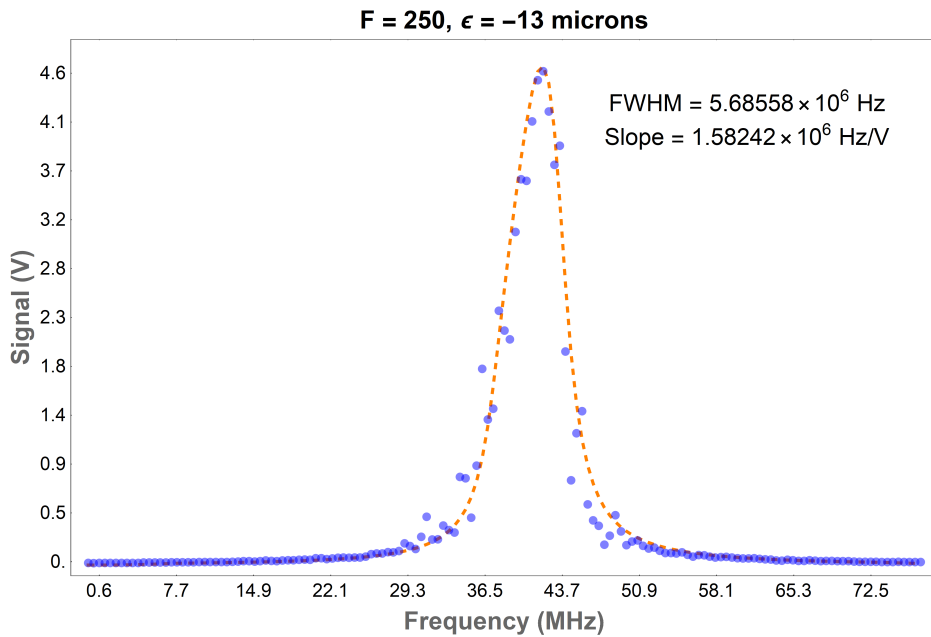


Figure 2.7: The trace of a cavity mode (data points in purple) seen on scanning the frequency of the *Matisse CS* was fit the custom function (Eq. 2.11), represented here by the dashed orange line, from which the width and slope of the line shape was extracted.

voltage ramp from an external signal generator to observe the cavity modes and zooming into the desired region on the edge of a peak, the side-of-fringe lock was achieved and the Network Analyser directed to measure the noise in the locked photodetector signal between 10 Hz to 1 MHz.

The noise spectra now at hand, it was essential to use them to better understand the frequency noise of the lasers which were both fully locked to the desired frequencies when the measurement was made. The trend, similar in the spectra for both the lasers, was a high noise level at the low frequencies from a 100 Hz which is just beyond the servo bandwidth with the level falling off in stages - first at around 550 Hz, then starts rolling down near 5 kHz after which it levels off close to 200 kHz. There were several prominent features visible, similar across the two spectra. A clear peak at 1 kHz is one which was easily attributable to the active Piezo Etalon that was being dithered at that frequency but the comprehension stops there, with no information regarding the origins of the other features. For this, multiple successive measurements were made by systematically disengaging the various locks starting from the tweeter/fast piezo locks and the woofer/slow piezo then the piezo etalon and thin etalon locks which revealed that the tall wide peaks near 10 kHz and 100 kHz were noise due to the action of the woofer and tweeter since they disappeared with the disengaging of the locks while naturally the 1 kHz bump disappeared with the Piezo Etalon being deactivated. These conclusions were justified with the reproducibility of the same features when the locks were re-engaged. The other peaks that could be distinguished from the fluctuations of small amplitude were labelled spurious since they did not correspond to any internal lock and were not reproducible. It was also noted in a separate frequency noise measurement with a low noise interference filter (IFL) laser, that the noise feature that spanned across the frequency range of 100 Hz to 1 kHz was present even in the noise spectrum of the IFL laser. Since the IFL laser is similar neither in form nor function to the *Matisse* lasers, this could be background noise from the cavity itself, perhaps due to mechanical vibrations. Piezo resonances are unlikely since the reported axial and radial resonance frequencies are 40 kHz and 65 kHz respectively. A dark noise measurement of the used photodetector showed no such noise pattern. Intensity noise could be another factor, though given the

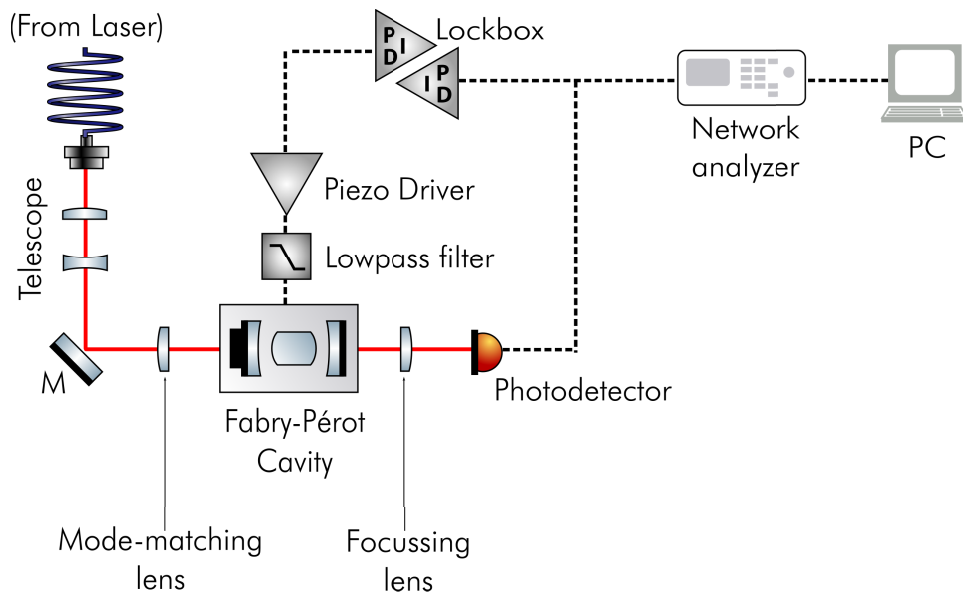


Figure 2.8: The frequency noise measurement setup.

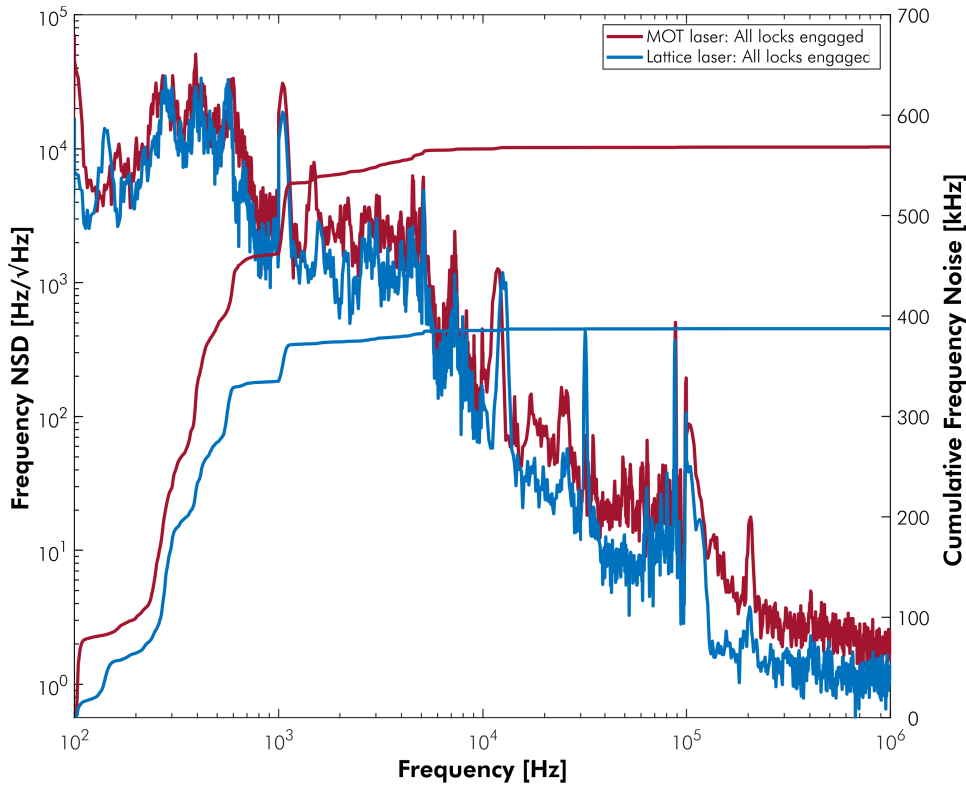


Figure 2.9: The frequency noise spectral density and the cumulative frequency noise of the *Matisse CS* and the *Matisse CR*.

measured intensity noise of the lasers and rescaling them with the conversion factor, it was found that their role, given the much larger frequency noise here, is actually negligible.

This noise measurement for the fully locked laser was done with no tweaking of the lock parameters of any element other than the tweeter whose integral gain was set to a 1000. Evident from the spectrum is that for this configuration, on the whole the noise level is low, especially in the critical range of frequencies between 1 kHz and 100 kHz. The same inference is drawn from the cumulative noise obtained by integrating over the noise spectrum with the most significant bump at 1 kHz due to the Piezo Etalon with no major rise beyond that. Unlocking the various elements naturally changed the overall noise level but the individual contributions remained the same. For the fully locked *CS* laser, it was noticed that while lowering the gain of the tweeter added to the noise, sending the maximum accumulated frequency noise from around 380 kHz at a gain of 1000 to 665 kHz at 500, increasing the gain to 2500 and beyond also added to the noise as well, taking the maximum cumulative noise to 403 kHz instead of further suppression. This suggested bounds for integral gain settings of the tweeter, with the ideal being 1000, since very little was attained by setting it to values between 1000 and 2500 while lower and higher values worsened the noise.

2.4.4 Estimation of laser linewidth from frequency noise

Taking the use of the frequency noise measurement a bit further, we can estimate the linewidth of the laser from the noise spectrum. Stating the laser linewidth is effectively another means of reporting frequency noise because of how the linewidth is determined by the noise. For the ideal case of only a pure white frequency noise spectrum, the line

shape is Lorentzian with the Schawlow–Townes–Henry linewidth. If the spectrum has 1/f or flicker noise in the lower frequency range it can cause a Gaussian broadening of the line shape [55]. If there is a combination of the 1/f-noise with the frequency-independent white noise that causes the Lorentzian line shape, it results in the Voigt profile [56]. While these can be arrived at analytically since it takes into consideration a rather simplistic nature of the noise, a measured noise spectrum as we have seen is much more complex and leads to a line shape that can be determined only numerically. In the face of such a problem, Di Domenico et. al. [57] provide a simple approximation to estimate the linewidth by showing that a noise spectrum can be geometrically separated in two regions with distinct influences on the line shape with only one region contributing to the linewidth and the other affecting only its wings. This is proven as follows - Given a frequency noise spectrum $S_{\delta\nu}(\nu')$, the autocorrelation function of the laser light field $E(t)$ can be written as [58],

$$\Gamma_E(\tau) = E_o^2 e^{i2\pi\nu_o\tau} e^{-2 \int_0^\infty S_{\delta\nu}(\nu') \frac{\sin^2(\pi\nu'\tau)}{\nu'^2} d\nu'} \quad (2.13)$$

where $\delta\nu = \nu - \nu_o$ is the laser frequency deviation around its average value ν_o . According to the Wiener–Khinchine theorem, the laser line shape is given by the Fourier transform of the autocorrelation function,

$$S_E(\nu) = -2 \int_{-\infty}^{\infty} e^{-i2\pi\nu\tau} \Gamma_E(\tau) d\tau \quad (2.14)$$

which cannot be analytically integrated for an arbitrary frequency noise spectrum but a simple rectangular noise spectrum, that is of constant value h_o till a cut-off frequency ν_c after which it is zero, can be considered. With this the eq. 2.14 is integrable for two limits: When $\nu_c \rightarrow \infty$, which gives a Lorentzian line shape with FWHM = πh_o and when $\nu_c \rightarrow 0$, which gives a Gaussian shape with FWHM = $(8\ln(2)h_o\nu_c)^{\frac{1}{2}}$.

This shows the spectrum has two regions which are radically different in how they affect the line shape. The regions are characterised by a modulation index β , defined as the ratio of the frequency deviation $\delta\nu$ to the modulation frequency ν , i. e., $\beta = \delta\nu/\nu$. One region is where this index is large owing to a high noise level compared to the modulation frequency and another where the index is small because of the lower noise. A dividing line called the β -separation line given by $S_{\delta\nu}(\nu') = 8\ln(2)\nu'/\pi^2$ helps identify the two regions. The noise components in the large modulation index area, typically in the lower frequencies, yield Gaussian autocorrelation functions which are multiplied together and then Fourier transformed give a Gaussian line shape whose variance is the sum of the contributions of all the high noise components. Conversely, the area of the high modulation frequencies but low noise and so small modulation index mean the modulation is too fast to have a significant effect on the laser linewidth. A reasonable approximation of the laser linewidth is therefore given by the following simple expression,

$$\text{FWHM} = (8 \ln(2) A)^{1/2} \quad (2.15)$$

where A is the area under the frequency noise spectrum in the high modulation index region or the overall area under the spectrum that exceed the β -separation line.

Using this expression, it was straightforward to calculate the laser linewidth of the *Matisse* lasers. For the *CS*, the β -separation line intersected the noise spectrum (more

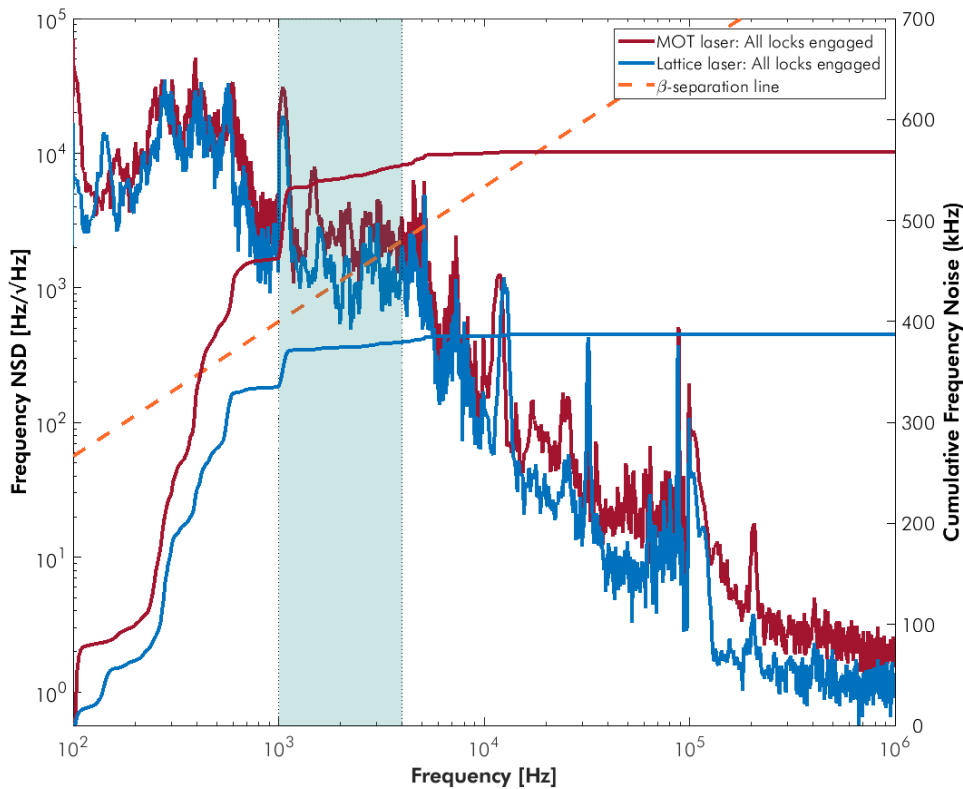


Figure 2.10: The linewidth estimation from the frequency noise is proportional to the area under the noise curve that lies in the high modulation index which is above the β -separation line (dashed orange line) shown here intersecting the curve at 4 kHz. A significant portion of the noise (between 100 Hz to 1 kHz) had to be ignored for this estimation since it was suspected that the noise is not of the laser's but perhaps coming from the cavity used for the measurement.

precisely, the smooth trendline that the spectrum was fit with to resolve the crossing frequency from the irregular, widely spread dataset) at 4 kHz which meant the spectrum above the line below this frequency had to be integrated over. Since a major section of this region was determined to come not directly from the laser but possibly the cavity, it was discarded with only the noise between 1 kHz and 5 kHz summed over and eq. 2.15 used to arrive at what was a lower bound on the linewidth of 104.8 kHz. Similarly for the *CR*, this was 217.6 kHz.

Reduction of laser linewidth

The laser linewidth could be reduced or in other words, the frequency noise of the lasers suppressed to a fair degree by tweaking the internal settings of the laser. While changing the integral gain of the tweeter was known to raise or lower the overall noise level, individual contributions from the active internal elements still needed to be addressed. Allowed by the available control was a tuning of one of these elements - the Piezo Etalon.

The Piezo etalon is essentially an optical cavity made of two tightly spaced prisms. The spacing between the prisms is actively controlled to match a multiple of the favoured longitudinal mode's wavelength so all except that mode have high losses and the etalon acts a mode filter. The control loop is based on a lock-in technique which measures the response of the laser to an externally induced perturbation which is a slight sinusoidal modulation of the etalon spacing at some frequency. This modulation can be controlled in

terms of its amplitude and phase shift. The tuning of these parameters are carried out to ensure the result of the convolution of the applied modulation waveform and the detected variation, which is the variation in the total laser power as measured at a photodetector, takes the shape of a double U to match the longitudinal mode position. This shape needs to be kept stationary and clean to an extent using the parameters.

The dither of the prism though contributes heavily to the frequency noise. To deal with this, the Piezo Etalon controller comes incorporated with a feed forward pathway that takes its own amplitude and phase shift values to model ahead the process dynamics and work to eliminate the noise. This feed forward was activated to serve that purpose but its parameters needed to be first optimised for efficacy for which the Fabry-Perót cavity, built to measure the frequency noise, proved handy. Acting as an optical spectrum analyser, the cavity was used to monitor the changes to the peak at 1.032 kHz, which is the set modulation frequency of the piezo etalon, as the feed forward parameters were varied to find the best values. This was done according to the procedure laid down by the manufacturer which was to start with a non-zero value for the feed forward amplitude then change the feed forward phase shift to match the modulation phase shift which should already have an effect. Following this, the feed forward phase shift alone should be altered for the lowest peak height before returning to varying the feed forward amplitude for further reduction. Noticing the decrease in the peak height in real time on the Network Analyser set to sample the spectrum of the cavity signal, a rescaled amplitude of 1.5 and a phase shift of 23.23° were settled on when the procedure was followed.

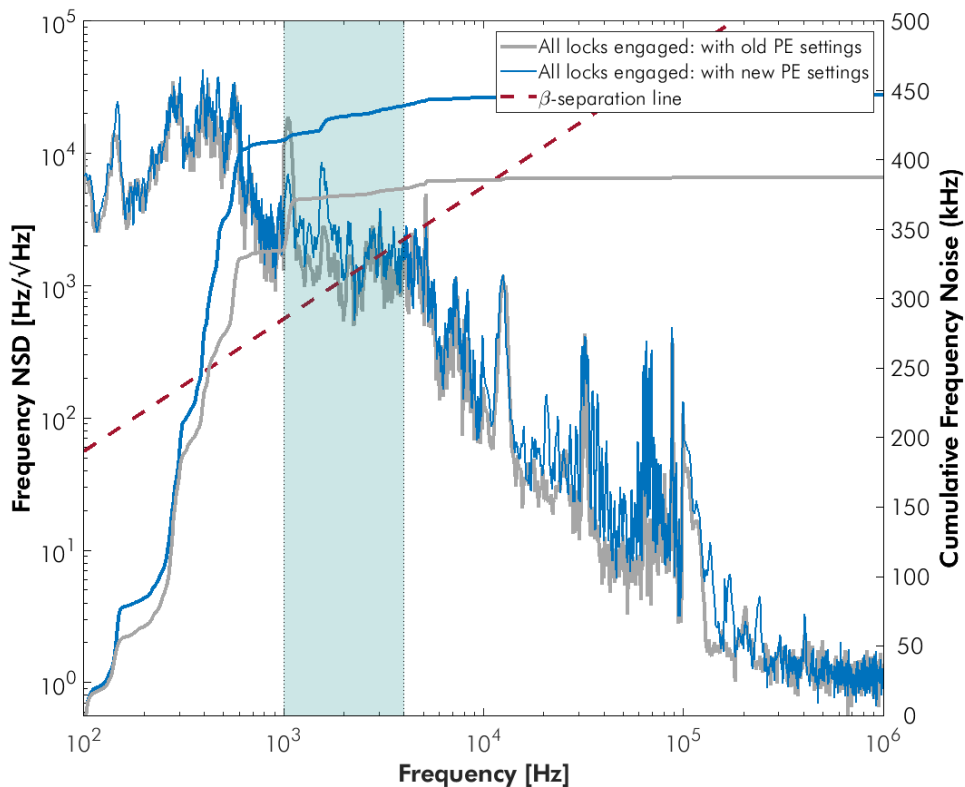


Figure 2.11: The linewidth of the *Matisse CS* was reduced from having a lower bound of 104.8 kHz to one of 58.64 kHz by decreasing the noise contribution of its active Piezo Etalon as is evident here with the smaller peak in the noise measurement (in blue) done after implementing the feed forward.

The linewidth of the *Matisse CS* extracted from the noise spectrum post activation and optimisation of the feed-forward showed a narrowing to 58.64 kHz with the spectrum itself showing a smaller peak at 1.032 kHz but with a new, short peak at 1.54 kHz. More glaring were other new features between the critical 30 kHz and 100 kHz. The root cause of this is as of yet unclear while it could be tied to the action of the woofer and tweeter over which the new noise appears. The origins of even their noise is currently unknown with only speculation of possible electronic noise in their drivers. Since the level remains low and there is also the likelihood of the noise being spurious, it stands to reason that the linewidth reduction can still prove to be advantageous especially from the perspective of unequal optical path lengths and the resulting position jitter due to this frequency noise.

2.5 FEEDBACK CONTROL VIA TRANSFER CAVITY

In addition to seeking suppression of the *Matisse CS* laser frequency noise in the mid-to-high frequency range, long-term frequency stability of the laser in terms of reduced drift would be ideal for experimental sequences which demand extended periods of stable operation. Although achieved to an extent out of the box, it was found that the stability could be enhanced further when the optical frequency of the laser output was noticed to drift by 50 MHz when monitored for a duration exceeding 12 h for which the proposal of extending the utility of the new Fabry-Perót cavity from a measurement device to a transfer cavity was made. Transfer cavities usually serve well to arrest long-term drifts. They are used to stabilize a target laser by “transfer” of the stability from a reference laser maintained at some frequency, usually determined by some suitable atomic transition. This can be accomplished one way by iteratively scanning the length of a cavity, searching for mode positions of the target and reference lasers, locking the cavity to the reference laser mode and then locking to one of the resonant modes of the target laser for the fixed (actively stabilised) cavity length, found again by scanning the target laser frequency. In another approach, the transmission maxima of both the reference laser and the target laser can be made to coincide at the same cavity length by frequency shifting either the reference or the target laser using an AOM. The cavity is then locked to the reference laser and the target laser is analog locked to the cavity forgoing any scanning of the cavity length.

Since this was meant to be a proof of principle and the former was a ready implementation, the latter approach was abandoned. Additional optics were added to steer a second beam into the frequency noise measurement cavity setup. To distinguish between the outgoing beams for the locking, the input beams needed to be polarised for which waveplates were added at both ends of the optical fibres bringing the light from the two lasers to the cavity setup. This was done to couple only one polarisation component of the laser beams into the fibres and then let through only that component to achieve high polarisation purity. Polarisers were added to aid in this effort. The beams were then directed through a polarising-beam-splitter (PBS) placed before the cavity with another placed after it. Two photodetectors were positioned to pick up light split between two perpendicular facets of the PBS depending on their polarisation. The *Matisse CR* laser locked to the D₂ line of Caesium for use as the cooler for the MOT was used as the reference laser to which then the cavity was locked. The signal from the photodetector

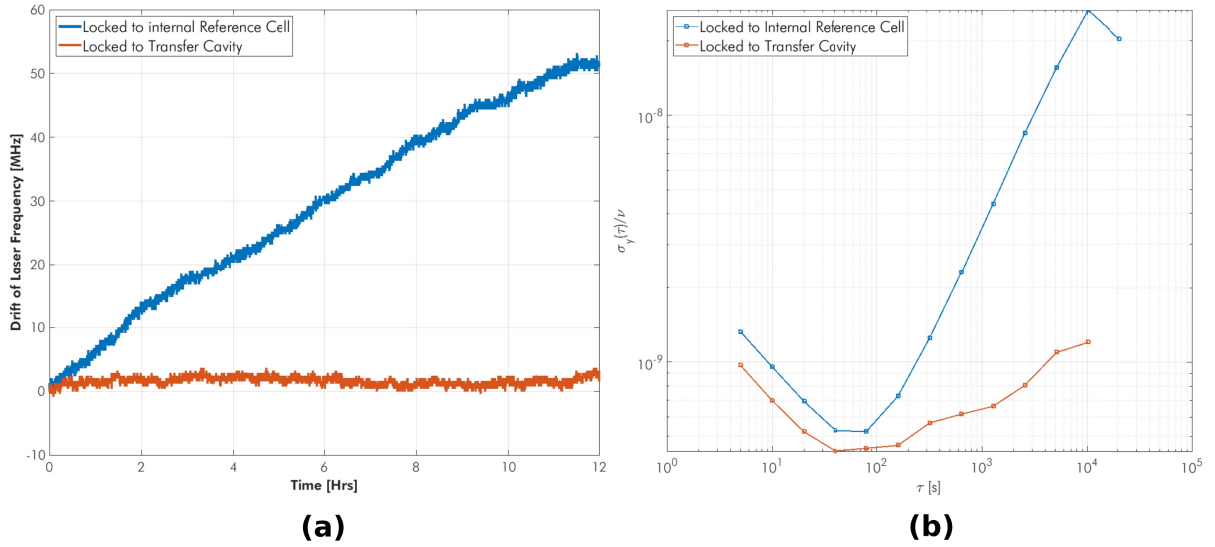


Figure 2.12: (a) Long-term stability of the *Matisse CS* before implementing the transfer cavity (in blue) and after (in orange). (b) The Allan deviation of the *Matisse CS* frequency before implementing the transfer cavity (in blue) and after (in orange).

picking up the light from the target *Matisse CS* laser was sent to the DSP input of the laser controller of the *CS* which offered the option of switching between its internal reference cell to an external cavity. This was used to have the controller achieve the same side-of-fringe lock of a cavity mode but this time of the modes of the transfer cavity.

A long-term measurement of the frequency of the *Matisse CS* now locked to the transfer cavity showed no consistent drift over time like earlier with only short-term excursions to a maximum of 3 MHz. The standard deviation of the frequency readout showed a drop from 11.07 MHz to 0.72 MHz. The Allan Deviation for the same was also found to reduce from a minimum of 5.282×10^{-10} at 40s sampling time to 4.363×10^{-10} at 40s also indicating the lower instability of the frequency of the laser locked to the transfer cavity.

3 | EQUALISATION OF OPTICAL PATH LENGTHS

The frequency noise can be stifled as shown with the fine-tuning of the laser source for the lattice beams but there remains a fraction of the noise that results in a relative phase difference due to the discrepancy in the path lengths. To eliminate this, as a first step, it is necessary to ascertain what set of paths need to be altered in length and by how much in order to achieve their equalisation, which for us is a near-nil difference between the paths. This chapter will present the conditions necessary to be met for the equalisation that were identified to help indicate the changes required. To then know of the existing path lengths, three methods for their measurement were used, each warranted by the limitations of the previous one - a direct geometric measurement, an optical measurement and finally a measurement using the trapped atoms themselves. Each of these measurements will be described in detail along with the results.

3.1 CONDITIONS FOR EQUALISATION

The quantified frequency noise can now be used to make a pragmatic estimate of the position jitter. The *Matisse CS* used for the lattice, with a lower bound on the reduced linewidth of 58.64 kHz gives a phase shift of 6.85×10^{-6} and so, using eq. 1.22 in Section 1.3.2, a position jitter of 0.47 pm. This is extraordinarily low even though this is also a lower bound calculated for the accumulated phase shift above 1 kHz and for a path length difference of just 1 cm. Since this is an order of magnitude smaller than our earlier assumed position jitter, a remarkable $\lambda/10^5$ stability can be achieved if the path length differences are brought to within even a metre of each other which is entirely feasible and so this remains our goal.

Equalising the beam paths leading up to the atoms from the source should involve only repositioning of a few optical elements and replacing, if necessary, any optical fibres along the way, however, the task is complicated by there being three lattice beams to generate the 2-D lattice and an additional two reference beams for the Optical Phase-Locked Loop (OPLL) that is present. All these beam paths need to be equalised among them, while also accounting for the OPLL and its action. This requires careful deliberation since there are now seemingly non-trivial equalisation conditions. To work our way to these conditions, we start by mapping out the relevant optical paths in the experiment.

Light from the same laser source - the *Matisse CS* - is split and distributed in to three 10 m fibres on an separate optical table and then brought over to the lower section of the experiment table where each is used for the 3 lattice beams, henceforth referred to by their assigned identifiers in the experiment, HDT1, HDT2 and HDT3 (where HDT stands for Horizontal Dipole Trap). HDT1 and HDT3 are the two counter-propagating beams with the HDT2 being the orthogonal beam. The HDT1 and HDT3 beams are polarisation synthesised, for which each of them is split further in to two paths of light with orthogonal polarisations and passed once through individual AOMs and then spatially recombined at

a Wollaston prism. The phases of these beams are stabilised by the OPLL since they are meant to be dynamically modulated in the experimental sequence in terms of their phase (and simultaneously intensity) using the AOMs with the assistance of a digital control system of which the OPLL is a part. The OPLL works by analysing separate beat signals between each of the HDT1 and HDT3 beams and two unchanged reference beams from the same source, which we shall call OPLL1 and OPLL2. In the experiment currently, these reference beams are split off from the HDT2 beam path before the HDT2 beam is also modulated by an AOM in single-pass. HDT2 is not phase stabilised and usually maintained to have a pure linear polarisation.

Following the polarisation synthesis setup, HDT1 and HDT3 are each coupled in to 2 m fibres and taken to the upper section of the table. HDT2 is also coupled in to a 2 m fibre after its AOM. Light for each arm coming with its respective orientation, after travelling through some more optics, goes past the window of the Mu-metal shielding and one face of the dodecagonal ultra-high vacuum glass cell within which the lattice is formed. OPLL1 is coupled in to a 2 m fibre and taken to the upper section where the beating with light picked off from the HDT1 beam path is carried out. OPLL2 is coupled in to a 5 m fibre and drawn across the lower section of the table to reach the otherside where it is beat with the HDT3 in the same manner.

In an abstract representation of the paths, which we call the *Connectivity graph* (Figure 3.1), we draw the beams as separate paths, sectioning them at relevant positions, to aid the formulation of the equalisation conditions -

- The OPLL1 beam path from its source A up to a point P' where the reference beam and the light picked off from the HDT1 beam is combined is assigned a length variable l_1 . The resulting beat is taken to the OPLL control electronics at B which since is a common path, is irrelevant.
- The HDT1 beam path from its source C up to a point D where light is picked off from this lattice beam to be combined with the reference beam is assigned a length l_2 .
- The path of the picked off light from the HDT1 beam between D and P' is assigned a length l_3 .
- The rest of the HDT1 beam path from D up to the window of the Mu-metal shielding at E is assumed to have a length l_4 , beyond which we assume for now the symmetry of the vacuum chamber and glass cell assures us of equal path lengths up to a few millimeters.
- The length of the HDT2 beam path extending from F to window of the Mu-metal shielding at G is taken to be l_5 .
- The HDT3 beam and its reference beam OPLL2 are sketched symmetrically to HDT1 and its reference to be assigned the lengths l_6, l_8 for the two sections HI and IJ of the HDT3 beam path while l_7 and l_9 are the given lengths for the picked off light from HDT3 along IP'' and the OPLL2 reference beam path KP'' respectively with the combined beam here going to its own OPLL control electronics at L .

Here A, F and K are the same source as setup currently in the experiment and there is the presumption that the intermediate paths introduced by the splitting of the HDT1 and

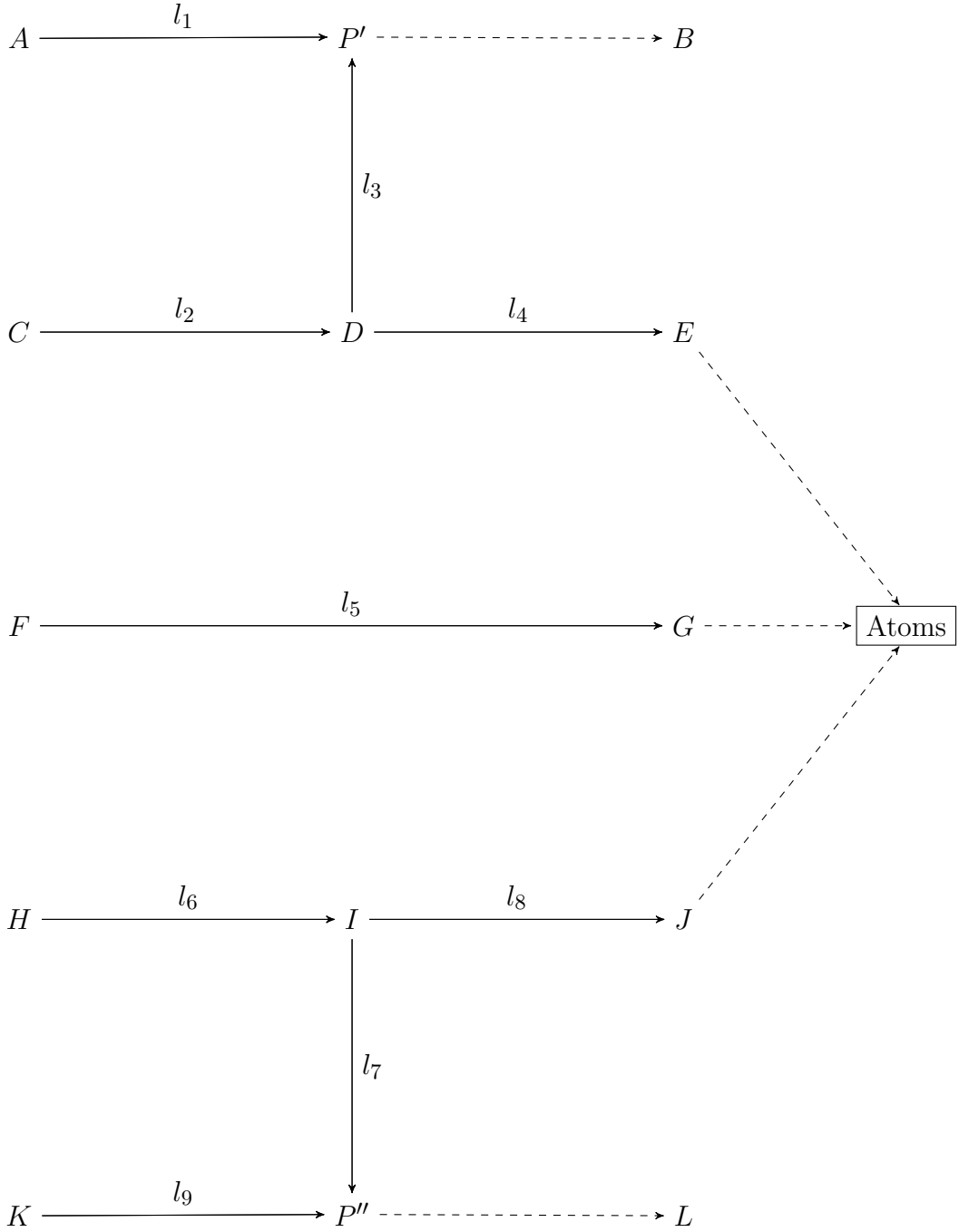


Figure 3.1: *Connectivity Graph*

HDT3 beams for the polarisation synthesis are commensurate which need not be the case. A simple algebraic restatement of the equalisation conditions can now be made which we call the *Constraint equations* for the path lengths. For completeness, we approach this treatment from the perspective of phase differences to incorporate not just the frequency noise but also the frequency shift caused by the AOMs in the path of the lattice beams and introduce simplifying assumptions to reduce them to a usable set of conditions.

3.1.1 Constraint equations

For a laser beam of optical frequency of ν and a frequency noise $\delta\nu$ traveling through the various paths, the phase difference between the pertinent sets of paths, as sketched in the *Connectivity Graph*, needs to be equalised. This constraint necessitated for each of those sets of paths can be written as,

$$(\nu + (80 \text{ Mhz}) + \delta\nu)(l_2 + l_3) = (\nu + \delta\nu)l_1 \quad (3.1a)$$

$$(\nu + (80 \text{ Mhz}) + \delta\nu)(l_2 + l_4) = (\nu + (80 \text{ Mhz}) + \delta\nu)(l_5) \quad (3.1b)$$

$$(\nu + (80 \text{ Mhz}) + \delta\nu)(l_6 + l_7) = (\nu + \delta\nu)l_9 \quad (3.1c)$$

$$(\nu + (80 \text{ Mhz}) + \delta\nu)(l_6 + l_8) = (\nu + (80 \text{ Mhz}) + \delta\nu)(l_5) \quad (3.1d)$$

Here,

1. Eq. 3.1a is an equality between the phase of the HDT1 beam coming along *CDP'* and the OPLL1 reference beam up to the point *P'* where they are combined for the OPLL. A difference in lengths between the two paths give rise to a phase difference under the influence of the noise which if is within its bandwidth, is visible to the OPLL which then actively compensates for it. In doing so this condition is met but this results either in a shift or opening up of the lattice.
2. Eq. 3.1b is for equal path lengths of HDT1 and HDT2 lattice beams up to the Mu-metal shielding window.
3. Eq. 3.1c is similar to the first equation but for the path length of the HDT3 beam coming along *HIP''* and the OPLL2 reference beam up to the point *P''* where they are combined.
4. Eq. 3.1d is for equal path lengths of HDT3 and HDT2 lattice beams up to the Mu-metal shielding window.

The actual optical frequency and the constant offset due to the AOMs where present can be ignored for this treatment (as will be done below) as they contribute only to the absolute, static phase at the position of the atoms while what is of greater importance here is the temporal fluctuations of the frequency $\delta\nu$. In the presence of the OPLL and its modulation of the phase, we can re-write only those equations from above which are relevant under each of the following three frequency regimes -

Low Frequencies - within the bandwidth of the OPLL

$$\delta\nu \cdot (\tilde{l}_2 + l_3) = \delta\nu \cdot l_1 \quad (3.2a)$$

$$\delta\nu \cdot (\tilde{l}_6 + l_7) = \delta\nu \cdot l_9 \quad (3.2b)$$

The OPLL will actively compensate for the phase fluctuations within its bandwidth which has been measured to be $\sim 200 \text{ kHz}$ by introducing a change in phase of the lattice beams. This can be regarded as some effective change in their optical path length represented here by \tilde{l}_2 and \tilde{l}_6 . This renders useless any equalisation between the three

lattice beams (if it has been carried out) due to this imprinted phase and results in undesirable shifts of the lattice.

Intermediate Frequencies - around the bandwidth of the OPLL

$$\delta\nu \cdot (l_2 + l_3) = \delta\nu \cdot l_1 \quad (3.3a)$$

$$\delta\nu \cdot (l_6 + l_7) = \delta\nu \cdot l_9 \quad (3.3b)$$

This is at the edge of the bandwidth of the OPLL where there could still be corrective action but perhaps not as pronounced as in the lower frequencies. We can assume here the changes to be small enough to leave the physical path lengths of the lattice beams and the reference beams effectively unchanged in magnitude but still disqualifies the other conditions.

High Frequencies - beyond the bandwidth of the OPLL

$$\delta\nu \cdot (l_2 + l_4) = \delta\nu \cdot l_5 \quad (3.4a)$$

$$\delta\nu \cdot (l_6 + l_8) = \delta\nu \cdot l_5 \quad (3.4b)$$

Here, the paths leading to and including the OPLL become irrelevant and so only the equalisation of the path lengths of the lattice beams need be considered.

It was learnt that it is practically tedious to change the lengths of certain paths like DP' (l_3) and IP'' (l_7) and the ones DE (l_4) and IJ (l_8) towards the atoms on the experiment table. The length of the HDT2 beam l_5 was also added to the list of path lengths to be left unrevised, partly since it was preferable but also for the reason that, one lattice beam should act as a reference to which the others can be equalised to. So fixing l_3, l_4, l_5, l_7, l_8 as constants would be convenient both practically and in this theoretical consideration to reduce the number of free parameters. The equations are also not all independent. Solving for the effective length and reworking the other conditions, this linear system of equations reduces to four expressions for the required physical lengths for the two lattice beams, HDT1 and HDT3, and the two reference beams OPLL1 and OPLL2 in terms of the now fixed lengths,

$$\delta\nu \cdot l_2 = \delta\nu \cdot (l_5 - l_4) \quad (3.5a)$$

$$\delta\nu \cdot l_1 = \delta\nu \cdot (l_5 - l_4 + l_3) \quad (3.5b)$$

$$\delta\nu \cdot l_6 = \delta\nu \cdot (l_5 - l_8) \quad (3.5c)$$

$$\delta\nu \cdot l_9 = \delta\nu \cdot (l_5 - l_8 + l_7) \quad (3.5d)$$

Since this brings together all the listed conditions, this should hold across all frequency ranges or equivalently, when the OPLL is active and when it is not. These expressions, which are but conditions for what the path lengths for the two lattice and reference beams should be for equalisation, can be used to conceive those lengths by elementary arithmetic provided the other fixed path lengths are known. To this end, having arrived at this during the course of our investigation, we moved on to quantifying the path lengths.

3.2 MEASUREMENT OF OPTICAL PATH LENGTHS AND DIFFERENCES

Measuring Optical Path Lengths (OPL) and particularly Optical Path Length Differences (OPLD) is an exercise often carried out in a variety of settings with numerous methods. Apart from the use of interferometry for direct measurement of the OPLDs [59], several indirect methods have also been developed like a time-of-flight technique wherein optical pulses are injected together into the two paths entirely inside fibres and the delay between the backscattered light in the fibre measured [60]. There are several reasons to choose one method over another based on factors such as the offered precision, sampling rate or time and cost efficiency in amount of materials put together to carry out the measurement. For our purposes, it is not necessary to be extremely precise since we have a wide tolerance on the required difference between the path lengths unless we wished to equalise the paths to within a few centimeters. The most straightforward methods were therefore used, as described below.

3.2.1 Geometric measurement

A good starting point was to carry out a geometric measurement of the optical path lengths in the experimental setup. This was a matter of noting the distances between all the optical elements where there is free space propagation and propagation through the fibres, taking care to account for the index of refraction for the two cases. The measurement procedure involved drawing a thread from edge to edge of the installed optics and measuring against a metre scale. This quickly proved to be tedious and given a very subjective estimate of error that varied depending on the tautness of the thread used for obtaining an accurate reading from the scale, it was not very precise. The error was also largely eclipsed by the stated fibre length tolerance which can be as large as 7.5 cm off from the nominal length. But the measurement was completed anyway (Figure 3.2), since it would still give us a reasonable estimate of the absolute path lengths which in conjunction with results of the more precise OPLD measurement methods can then be used to propose new lengths for the two lattice and reference beams.

3.2.2 Optical measurement through FMCW interferometry

Originally developed for use with the Radar and later found application in precision metrology, Frequency-Modulated Continuous-Wave (FMCW) Interferometry is a ranging technique that extracts distance from the frequency of the interference or temporal beat signal of a signal wave with a frequency-modulated waveform following its traversal through a path or a set of paths. Its optical variant works exactly on the same principle as the Michelson interferometer, with only the optical frequency of its light source being modulated at a set rate across a known range. The reason why this can be used to extract OPLDs is because the modulation of the frequency results in a time varying phase $\phi(t)$. The difference between this phase of each of the two interfering waves results in a

sinusoidal beat signal $I(\tau, t)$ given some temporal delay τ between the two waves which can be due to the OPLD between the paths traversed by the two waves,

$$I(\tau, t) = I_o(1 + V \cos(\phi(t) - \phi(t - \tau))) \quad (3.6)$$

where if I_1 and I_2 are the intensities of the two interfering waves, $I_o = I_1 + I_2$ is the total intensity and $V = 2\sqrt{I_1 I_2}/(I_1 + I_2)$ is the contrast of the beat signal. This beat signal is visible without washing out in the first place, only if the initial phases of the interfering waves are correlated (that is, if for instance, the two waves are derived from the same coherent modulated optical source but travel along different paths before they meet).

Optical FMCW interferometry was then the second method to be used to determine the OPLDs in the experiment between paths for beams which were beaten with each other while scanning the laser over several GHz at a fixed rate. Since the lattice beams HDT1 and HDT3 were already being combined with the reference beams to generate a beat signal for the OPLL, the same signal was used to carry out the FMCW interferometry, taking care to down-mix the beat signal with an external 80 MHz reference and low-pass filter it (Figure 3.3) to extract the beat oscillations due to the difference in path lengths which were at the low frequencies. The beat corresponding to one edge of the ramp applied to the laser frequency was then fit with a sinusoid and the beat frequency ν_b determined. Knowing the range of frequency scanned $\Delta\nu$ and the rate $1/T$, the OPLDs were calculated with the formula (see Appendix A),

$$\text{OPLD} = \frac{\nu_b c}{\Delta\nu/T} \quad (3.7)$$

The paths of HDT1 and HDT3 are actually split for discretionary control of the orthogonal polarisation components in the polarisation synthesis setup (and called HDT1L/R, HDT3L/R). The two components of each arm travel separate paths in this setup and then are recombined to be sent to the atoms. The components are again separated to generate separate beat signals for the OPLL which were all individually used to measure the OPLDs (Figure 3.4(a) shows one such measurement). The difference in the paths of the two components in the polarisation synthesis setup was also measured (Figure 3.4(b)). This was done by observing the recombined signal behind a polariser while scanning

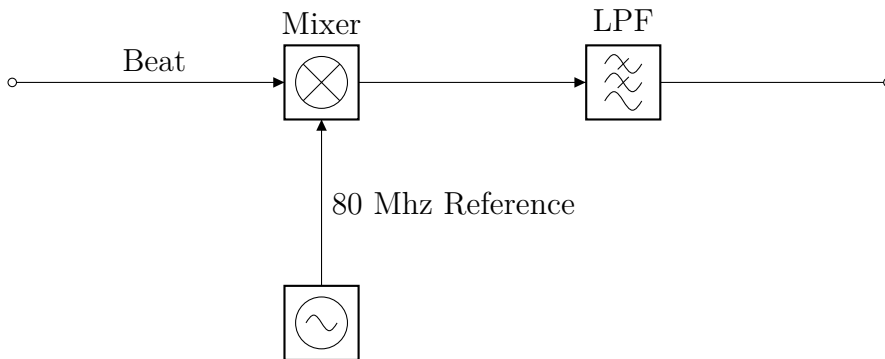


Figure 3.3: The beat signals involving those beams shifted in frequency by the AOMs were down-mixed with an external 80 MHz reference and low-pass filtered when employing FMCW interferometry

the frequency of the laser. In the theoretical analysis we had assumed the two paths to be equal but this optical measurement showed (as was also evident with the geometric measurement), that was not the case.

Comparing the results of this measurement with the values for the differences between the same paths as calculated from the geometric measurement data (Table 3.1), the optically measured differences were found to be off by a minimum of 4% but as large as 14%. Being an optical measurement and given the drawbacks of geometric measurement, the Optical FMCW interferometry was ultimately more precise. This method is also naturally a ready visualisation tool for the existing OPLDs with the observed beat frequencies being higher for larger OPLDs and lower for smaller ones and so can be used for a more refined adjustment of path lengths when it is carried out.

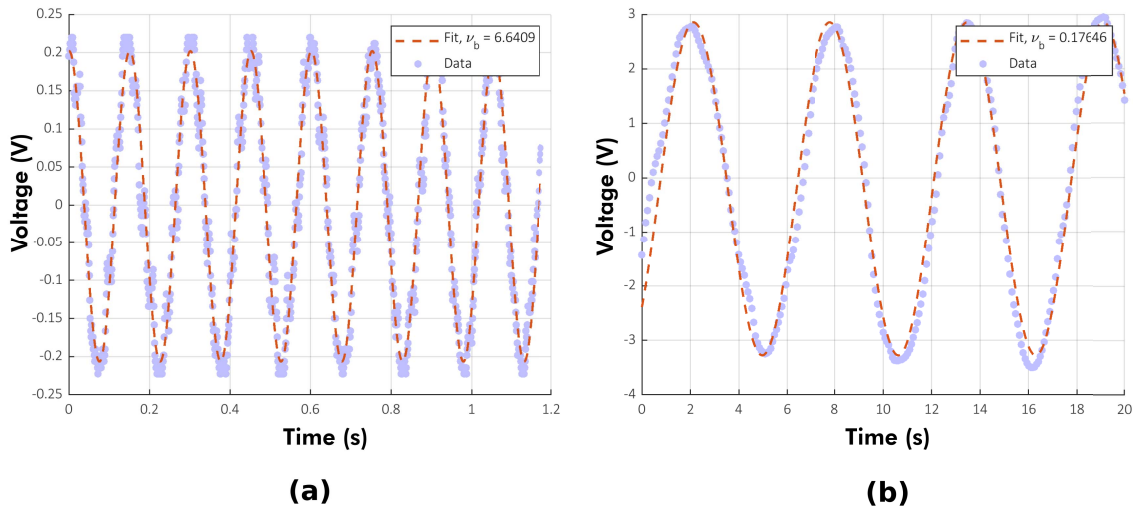


Figure 3.4: (a) Beat signal as observed between HDT3R and OPLL2 - the beat frequency extracted from the fit was 6.64 Hz which gave an OPLD of 4.185 m according to eq. 3.7 for a scan across 12 GHz at 0.5 GHz/s. (b) Beat signal as observed between HDT3L and HDT3R - the beat frequency extracted from the fit was 0.176 Hz which gave an OPLD of 0.062 m for a scan across 26 GHz at 0.8 GHz/s.

OPLD	Geometric measurement (cm)	Optical measurement (cm)	Error (%)
HDT1L - OPLL1	50.5 ± 16	43.4	14.0
HDT1R - OPLL1	46 ± 16	41.7	9.3
HDT3L - OPLL2	386 ± 16	402	4.0
HDT3R - OPLL2	392 ± 16	418.5	6.8
HDT1L - HDT1R	4.5 ± 3	4.7	4.4
HDT3L - HDT3R	5.5 ± 3	6.2	12.7

Table 3.1: Measured differences using geometric and optical methods along with the error indicating how far off the optically measured value is from the geometrically measured value.

3.2.3 Measurement using atoms

We had to this point utilised two methods for the same measurement and yet not quite hit the mark - The geometric method, now already superseded by the optical measurement in terms of precision, had allowed measurement only up to the Mu-metal shielding and not beyond. The optical measurement proved to be useful to measure differences between path lengths but only at points where a beat signal could be generated. Left wanting for a more complete picture with the OPLDs measured up to the position of the atoms with the required precision, atoms themselves were thought of as a tool to achieve this by measuring their shift along with the lattice they were trapped in, that would shift under a fluctuation in frequency because of the OPLDs. Exaggerating this fluctuation by deliberately ramping the frequency to produce this shift of atoms, became the third method used to then extract the OPLDs while helping make for a compelling demonstration of unequal path lengths on any final measurements involving atoms in the experiment.

Calibrating the atom images

The use of the atoms to measure OPLDs meant processing datasets of images of the trapped atoms. In a typical experimental sequence an illumination beam (an 852 nm laser beam in the experiment) is shone on the atoms to have them fluoresce. The fluorescence light is collected by an objective lens and focused on to an Electron-Multiplying Charge Coupled Device (EMCCD) sensor that renders a digital image. To use these images to determine the OPLDs by measuring the shift of the atoms required,

- Determining the direction from which the lattice beams entered to form the 2-D lattice in the field of view of the camera and identify each beam: The EMCCD camera, centered on the region where the HDT1, HDT2 and HDT3 beams form the lattice within the science chamber, is oriented in a manner that any shifting of atoms which will be along the diagonals of the lattice will show as a shift along the horizontal and vertical axes of the image. The actual direction from which the three beams enter the region of the object plane, however, was ambiguous.
- An algorithm that can detect subpixel movement and report the shift in distance units with the correct conversion factor.

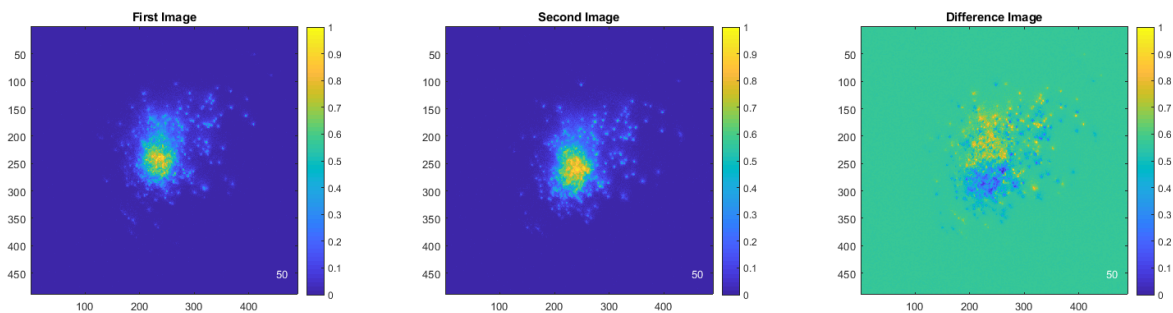


Figure 3.5: State-independent transport of atoms carried out by changing the phase of both polarisation components of HDT3. This resulted in a downward shift as is clearly visible here in the difference between the images before and after transport over 16 lattice sites.

The orientation of the counter-propagating HDT1 and HDT3 was learnt very easily - noticeable when HDT2 was turned off or blocked and loading atoms on to the 1-D lattice that forms, the atoms were seen clearly trapped along the direction of the principal diagonal of the image matrix. The HDT1 and HDT3 beams were therefore along the other diagonal of the image with the HDT2 along the principal diagonal but this still did not definitively identify each beam. It also did not unambiguously fix the direction of HDT2 along the principal diagonal. This prompted the use of deterministic shifting of the atoms facilitated by polarisation synthesis of the HDT1 and HDT3 beams to carry out (state-independent) transport and track the direction of atoms as they moved along the principal axes of the lattice for the pre-determined rotation of polarisation of each beam.

In parallel, the algorithm for detecting the shift in the atoms was developed. The transport sequence as carried out in the lab involved loading the atoms in to the lattice and taking a first image, then transporting the atoms by changing the phase of one of the synthesised beams (more accurately, for state-independent transport, the phase of both the polarisation components of either HDT1 or HDT3 was changed). A second image was taken after the transport before finally taking a background image to subtract possible noise or stray light from the first two images. During the sequence some other beams can be optionally toggled to be actively shining on the atoms like the Vertical Dipole Trap beam (VDT) as was done when the atom transport sequence was run. This meant that the atoms were drawn to VDT beam position where they clustered disallowing detection and tracking of individual atom position. It was still possible to track shifts between the first image before transport and second image after transport despite the atoms visible only as a cloud by the technique of cross-correlation of the images as is commonly done in the field of image processing and goes by the label of image registration.

Cross-correlation of one $M \times M$ matrix with an $N \times N$ matrix is carried out by sliding one of the matrices across the other and summing up element-wise products to generate a $(M + N - 1) \times (M + N - 1)$ cross-correlation matrix. In doing this of the image matrices in the domain of pixel intensity values, the cross correlation "undoes" any shift between the images and the position of the maximum value in the cross-correlation matrix corresponds to the position where there is the most similarity between the images. The shift is then obtained by taking the difference of the peak position in cross-correlation matrix from the peak position in the *auto*-correlation matrix, which is similar to cross-correlation only that it is carried out with the same image, here of the first image. This gives the amount of pixels (since each element of the image matrix is one pixel) by which the features of the first image have shifted by in the second image. The actual cross-correlating of the matrices was carried out by using an in-built MATLAB function for 2-D cross-correlation called *xcorr2*. A time-efficient alternative to this algorithm was later found in an implementation by Guizar-Sicairos et al., working on the same principle of cross-correlation but in the frequency domain [61]. This was used particularly when there were large datasets to be processed and with the claim of being able to resolve at a sub-pixel level, was arguably a better choice to detect miniscule shifts where it is anticipated.

In one transport dataset that was acquired, the phase of the HDT3 beam was modulated to shift the atoms by fixed amounts of lattice sites (Figure 3.5). The shift was determined using the cross-correlation but in terms of pixels which needed to be converted to lattice sites. The conversion factor from pixels to lattice sites is theoretically derived by calculating first the magnification from the focal lengths of the objective lens ($f = 11.96\text{mm}$) and the later focusing lens ($f = 500\text{mm}$) before the camera and was found to be 41.8. Each pixel

of the EMCCD has a size of ($16\mu\text{m}$) which would mean it would capture 382nm of the object plane. If the lattice spacing is $\lambda/\sqrt{2}$ (as is the case for the 2-D lattice), each pixel corresponds to 1.6 lattice sites. Using this number, the measured shifts were found to fall on a straight line against the expected shift as programmed. This justified the use of the cross-correlation technique but the agreement was not exact. This was perhaps because the used value of magnification was different from the actual value which was determined by fitting a line to the shift data and was found to be 44 giving a magnification factor of 1.7 (Figure 3.6).

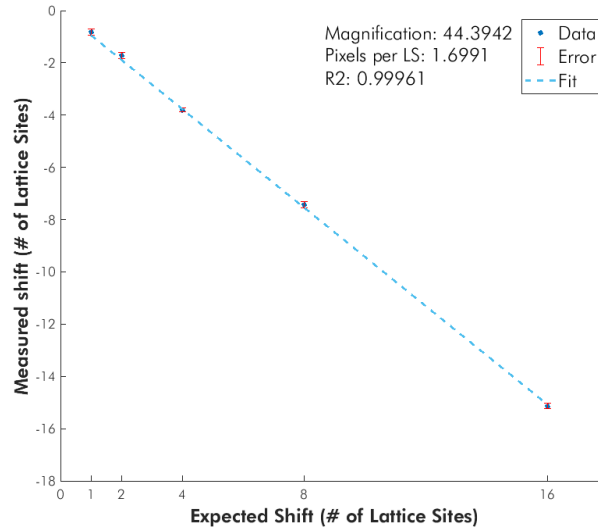


Figure 3.6: Measured shift fell in line with the expected shift. The linear fit though suggested a slightly different magnification than the value calculated from knowing the focal lengths of the objective and focusing lens before the camera.

Returning to the question of the identification of the beams, the modulation phase of the HDT3 was done first in the increasing direction. The observed shift of the atoms as they were transported for this change of phase showed a movement down along the vertical axis of the camera image. Decreasing the phase showed a movement up along the vertical. Doing the same with the phase of the HDT1 beam showed a movement along the horizontal first to the right for increasing phase and left for a decreasing phase. Knowing the translation vectors for transport on this synthesised 2-D lattice (see Section 1.2), it was now clear that the beam from the lower left corner of the image is HDT3, the upper right is HDT1 and the only possible direction HDT2 entered the field of view was from the upper left corner.

Measuring OPLDs from the shift of trapped atoms

With the protocol to measure the shifts of the atoms now laid down, the laser frequency was scanned to shift the lattice corresponding to the OPLDs between the beams. The scanning of the laser frequency was carried out by sending a digital trigger at the required moment in the sequence via a *National Instruments USB-6000* DAQ board connected to a second lab PC. An active MATLAB script on that PC picked up on the trigger state to send commands over a serial port to the *Matisse CS* laser controller with the help of a custom class written for communication with the laser. The commands sent were to switch to scanning the laser frequency using the reference cell over first a wide range of optical frequencies in one direction (which meant having to re-scan the laser to its initial

position during every run of the sequence) at the fastest rate possible, without having the laser fall out lock. The programmed experimental sequence was as follows,

1. Load atoms in 2-D Lattice
2. Take the first image of atoms in 2-D lattice
3. Start scanning of laser frequency in one direction on trigger HIGH
4. Wait for a few seconds
5. Take the second image of atoms in 2D lattice
6. Take the background Image
7. Start scanning back laser frequency to initial value on trigger LOW

For this measurement, there was the issue of the action of the OPLL to consider. During other experimental sequences such as transport, the OPLL was necessarily active. When measuring path length differences, as argued earlier, there are different cases which for this measurement was simply taken to be - the OPLL being active for both HDT1 and HDT3 and the OPLL inactive for both with an additional case of the OPLL being active for one of either HDT1 or HDT3.

Using the constraint equations, it can be shown that for the case of the OPLL being active for both HDT1 and HDT3, due in part to the long reference beam fibre used for HDT3, the effective path length differences will be large and so will therefore, the resulting shift of the atoms when the laser frequency is scanned. This prediction was tested by running the above sequence with the laser being scanned over 1.7 GHz at nearly 1 GHz/s in one direction (up from lower to higher frequencies) and collecting statistics (50 runs of the sequence were recorded) (Figure 3.7). The scanning was monitored using a *High Finesse* wavemeter to ensure the scanning was linear for the most part and there were no mode jumps. The shifts measured by cross-correlation of images were noted along both the horizontal and vertical directions since this was on the 2-D lattice and there would be a net translation of the atom cloud due to the pairwise OPLDs between the lattice beams - the HDT1 with HDT2 and HDT3 with HDT2 - and the translation would be along the same respective vectors as in the transport experiment. Calculating the corresponding OPLD for the measured shift of the atom cloud along those directions and comparing with the expected OPLD as estimated using the geometric measurement data, it was found that there indeed was a large shift especially in the vertical direction because of an OPLD in excess of 3 m between HDT3 and HDT2 (Table 3.2). While there was agreement between the expected and measured OPLD between HDT3 and HDT2 to within 5%, the same could not be said of HDT1 and HDT2 for which the measured OPLD was off by 83%.

The reasoning for this currently remains a conjecture. It is possible that the expected OPLD is a gross overestimation due to the inherent imprecision of the geometric measurement. It could also be that the shift in the direction of the posited large OPLD was much more dominant and won over a shift in the other direction.

The other cases of the OPLL state - being inactive for one or both counter-propagating beams - were also tested. When the OPLL was made inactive for HDT1, atoms were completely lost from the lattice following the scan. This is perhaps explained by the

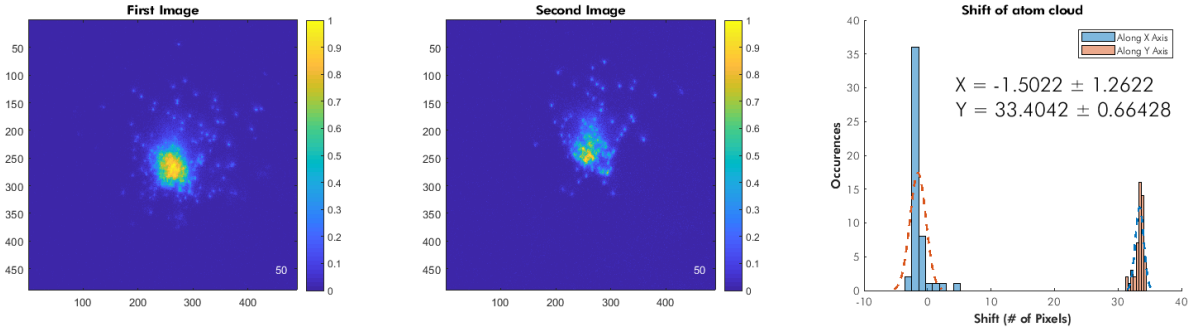


Figure 3.7: Images of trapped atoms before (first image) and after (second image) the scanning of the laser frequency with the OPLL active for both arms alongside the distributions of the shift of the atom cloud in the horizontal (here called the X-axis) and the vertical (called the Y-axis).

OPLD	Expected OPLD (cm)	OPLD measured from shift of atoms (cm)	Error (%)
HDT1 - HDT2	95 ± 16	16 ± 2	83
HDT3 - HDT2	334 ± 16	349 ± 1	4.5

Table 3.2: Measured OPLDs using the geometric method and from the measurement using atoms along with the error indicating how far off the latter value is from the geometrically measured value.

non-zero OPLD between the paths for the orthogonal polarisation components of HDT1 which combined with the large OPLD, due to the active OPLL for HDT3, opened the 2-D lattice by moving the sublattices relative to each other that excited the atoms away. The same was not true when only HDT3 was made inactive because there was no large OPLD due to an active OPLL for HDT1 but there was still enough atom loss to broaden the distributions of shifts along the two directions. Deactivating the OPLL completely for both, also yielded similar results.

Further inquiry is required to explain these preliminary observations. There is also a need to resolve the several issues by modification or improvement of the measurement sequence, for instance, in terms of better retention of atoms in the lattice, which even in the case of fully active OPLL can be poor because of the scan duration which is in seconds. Here, the cross-correlation has no clear peak and the shift is undetermined.

OUTLOOK

From their inception, lasers have proven to be remarkably felicitous in what has become an endless quest for broadening the horizons of technology. But it is by ushering in the new quantum age of the same, that lasers have revealed their true prowess. While yet to find similar use beyond the laboratory, the fine control and manipulation of matter enabled by the lasers in a manner inconceivable without their existence has deepened our understanding of quantum phenomena. This has been achieved to an extent that we can exploit some to supplement classical machinery otherwise limited in scope to carry out tasks more efficiently on different fronts or even probe new science. This is the motivation behind experiments such as DQSIM (Discrete Quantum SIMulator) in Bonn with the core objective to implement quantum walks of cold atoms on an optical lattice. The laser is not without its limitations however and it is up to the experimenter to identify possible impediments and comment on the size of their role apropos of the experiment. This was the goal of this thesis with an extensive inquiry centered on the laser noise, with a focus on laser frequency noise.

Frequency noise was identified as one way in which atoms can get heated out of the lattice in which they are trapped, necessitating their quantification. This was done for two new lasers that were acquired for the lab, in addition to their smooth integration in to the experiment. The manner in which the noise measurement was accomplished was with the use of an optical frequency discriminator like a Fabry-Perót cavity. A cavity was built with a four-fold increase in transmission of existing cavities for this purpose. In the course of building the cavity, the classic optics problem of spherical aberration was come across which despite being pervasive and having been studied in the context of cavities decades prior, rarely finds mention in most practical descriptions of cavities. This understanding particularly helped in more precisely calibrating the device for measuring the frequency noise of the lasers which was done using the side-of-fringe locking technique. The measured frequency noise spectrum revealed how some internal components of the lasers contributed to noise. This was then used to reduce the magnitude of the noise (of one laser used as a source for the optical lattice) by fine-tuning and noting optimum values for the parameters that go in to determining the laser operation. Post its use a device to measure the frequency noise, the Fabry-Perót cavity was put to use as a transfer cavity to also improve its long-term stability.

In both as a frequency noise measurement device and a transfer cavity, a substantial factor in terms of the quality of performance of the Fabry-Perót cavity is its mechanical stability. In its current realisation, the cavity is not completely guarded against external influences of acoustic vibrations or thermal fluctuations. Some improvements in design can be made to correct for this shortcoming such as introducing rubber damping elements at critical mounting locations of the mirror, piezo or between the entire cavity and the table it is installed on which is not devoid of vibrations from the surrounding equipment that can couple in to the cavity. Thermal fluctuations are a problem to a smaller degree considering the stable temperatures in the lab and any local changes in temperature can be avoided by careful placement of the cavity on the table. Another solution to completely eliminate any thermal influence would be to replace the cavity housing and the internal

metal mounts by one made of a material with low thermal expansion coefficient but this is mostly unnecessary. More elegant and possibly less noisy implementations of the mirror actuation over the use of a piezo as used currently with the mirror glued directly on to the piezo tube can also be sought.

The frequency noise makes its presence known through the Optical Path Length Differences (OPLDs) in the experiment. The second phase of the thesis was therefore naturally dedicated to their measurement and elimination as well. The conditions required to be met for minimal OPLDs or simply, equalisation, were first derived. With measured OPLDs, the equalisation conditions become useful to determine what certain path lengths should be but since the task of measuring the OPLDs itself was found to be not entirely straightforward, requiring three different methods, the actual task of bringing the path lengths to the desired values still remains.

The results of the last of the three OPLD measurement methods that involved the use of the atoms, is yet to be interpreted and understood in its entirety. To improve first its reliability, one suggestion is to disable the use of the Vertical Dipole Trap (VDT) during the laser scanning sequence to prevent atom clustering. This would also allow the atoms to oscillate between multiple planes without tight vertical confinement which, since it will not affect how their dynamics on the horizontal lattice, should only allow for improved resolution to detect their movement as they get dragged along with the shifting lattice. The atom loss due to the long scan duration can be perhaps reduced with constant cooling using the molasses beams. The future roadmap is then clear with regard to the project of the equalisation of paths. There is first the repeating of the measurement using the atoms with changes like mentioned above following which a combination of the interferometric technique and the atomic measurement can be used to equalise path lengths by readjusting optical elements or replacing fibres with as little disruption as possible. Another task which is also pending is the installation of Photonic Crystal Fibres to make full use of the high powers that the new lasers offer, which should be managed in the coming months.

A | APPENDIX

A.1 PRINCIPLE OF OPTICAL FMCW INTERFEROMETRY

Presented here is an analytic argument for the use of Frequency-Modulated Continuous Wave (FMCW) interferometry extending from [62] and put in the context of measuring the optical path length differences in the 2-D experiment.

Consider one each of the reference E_1 (with an initial phase ϕ_1 , k -vector \mathbf{k}_1) and the lattice beams E_2 (with an initial phase ϕ_2 , k -vector \mathbf{k}_2) having their frequencies modulated with say a triangular wave around a center frequency f_o at a rate α given as,

$$E_1(\mathbf{r}, \tau, t) = E_{01}e^{i((\alpha t + 2\pi f_o)t - \mathbf{k}_1 \cdot \mathbf{r} - \phi_1)}$$

$$E_2(\mathbf{r}, \tau, t) = E_{02}e^{i((\alpha(t - \tau) + 2\pi(f_o + 80\text{Mhz}))t - \mathbf{k}_2 \cdot \mathbf{r} - \phi_2)}$$

τ is the delay time of the lattice beam with respect to the reference beam which could be the time needed to travel the extra distance if there is a difference in the lengths of the paths (OPLD) of the two beams, so $\tau = \text{OPLD}/c$. As is evident, the 80 Mhz shift introduced by the Acousto-Optic Modulator (AOM) to the lattice beam is also included. The 2 waves are combined after which they travel in the same direction (say x). The resulting beat signal (more precisely the time averaged beat signal) can therefore be written as,

$$I_s(x, \tau, t) = |E_1(x, \tau, t) + E_2(x, \tau, t)|^2$$

$$= E_{01}^2 + E_{02}^2 + 2E_{01}E_{02}\text{Cos}(\alpha\tau t + (2\pi(f_o - (f_o + 80\text{Mhz})))t - (k_1 - k_2)x + \Delta\phi)$$

$$= (\text{constant offset}) + I_1\text{Cos}(\alpha\tau t + (2\pi(f_o - (f_o + 80\text{Mhz})))t - (k_1 - k_2)x + \Delta\phi)$$

where $\Delta\phi = \phi_1 - \phi_2$. If a photodetector is placed on the plane perpendicular to the x-axis, a purely temporal signal can be obtained. The spatial dependence can be absorbed in to a phase term as some error for the reason that -

$$(k_1 - k_2)x = \left(\frac{\omega_1}{c} - \frac{\omega_2}{c}\right)x$$

$$= \left(\frac{\alpha t + \omega_o}{c} - \frac{\alpha(t - \tau) + \omega_o}{c}\right)x$$

$$= \frac{\alpha\tau}{c}x$$

$$= \frac{\Delta\omega \text{ OPLD}}{T c^2}x$$

which is a small number even for scans in the GHz range and distances in the few metres. This beat signal can then be mixed down with an RF source and the difference frequency isolated with a low pass filter,

$$\begin{aligned} I_s(\tau, t) &= I_1 \text{Cos}(\alpha\tau t + (2 \pi (f_o - (f_o + 80\text{Mhz})))t + \phi_{b0}) \\ I_r(t) &= I_2 \text{Cos}((2 \pi 80\text{Mhz})t + \theta) \end{aligned}$$

where, $\phi_{b0} = \Delta\phi - (k_1 - k_2)x$.

$$\begin{aligned} I(\tau, t) &= I_s(\tau, t) \cdot I_r(t) \\ &= I_1 I_2 \text{Cos}(\alpha\tau t + (2 \pi (f_o - (f_o + 80\text{Mhz})))t + \phi_{b0}) \cdot \text{Cos}((2 \pi 80\text{Mhz})t + \theta) \\ &= \frac{I_1 I_2}{2} \text{Cos}((2 \pi 160\text{Mhz})t + \theta - \alpha\tau t - \phi_{b0}) \cdot \text{Cos}(\alpha\tau t + \phi_{b0} + \theta) \\ &\stackrel{\text{LPF}}{=} \frac{I_1 I_2}{2} \text{Cos}(\alpha\tau t + \phi_{b0} + \theta) \\ &= \frac{I_1 I_2}{2} \text{Cos}(\omega_b t + \phi_{b0} + \theta) \end{aligned}$$

Here,

$$\begin{aligned} \omega_b &= \alpha\tau \\ \alpha &= \frac{\Delta\omega}{T} \\ \tau &= \frac{\text{OPLD}}{c} \end{aligned}$$

$$\implies \text{OPLD} = \frac{\omega_b c}{\alpha} = \frac{\nu_b c}{\Delta\nu/T}$$

ν_b is the frequency of the beat signal observed when the optical frequency is scanned over a range $\Delta\nu$ in a period T . The above expression is then how the OPLD can be calculated.

BIBLIOGRAPHY

- [1] J. Quintanilla and C. Hooley, *Physics World* **22**, 32 (2009).
- [2] S. Sachdev, *Nature Physics* **04**, 173 (2008).
- [3] R. P. Feynman, *International Journal of Theoretical Physics* **21**, 22 (1982).
- [4] S. Lloyd, *Science, New Series* **273**, 1073 (1996).
- [5] I. Bloch, J. Dalibard, and S. Nascimbène, *Nature Physics* **8**, 267 (2012).
- [6] R. Blatt and C. F. Roos, *Nature Physics* **8**, 277 (2012).
- [7] J. Q. You and F. Nori, *Physics Today* **58**, 42 (2005).
- [8] A. Aspuru-Guzik and P. Walther, *Nature Physics* **8**, 285 (2012).
- [9] M. J. Hartmann, *Journal of Optics* **18**, 104005 (2016).
- [10] T. Byrnes, N. Y. Kim, K. Kusudo, and Y. Yamamoto, *Physical Review B* **78**, 075320 (2008).
- [11] Y. Wang et al., *ACS Nano* **9**, 7769 (2015).
- [12] I. Bloch, J. Dalibard, and W. Zwerger, *Reviews of Modern Physics* **80**, 885 (2008).
- [13] R. Grimm, M. Weidemüller, and Y. B. Ovchinnikov, in, Vol. 42, edited by B. Bederson and H. Walther, *Advances In Atomic, Molecular, and Optical Physics* (Academic Press, 2000), pp. 95–170.
- [14] D.-W. Zhang, Y.-Q. Zhu, Y. X. Zhao, H. Yan, and S.-L. Zhu, *Advances in Physics* **67**, 253 (2018).
- [15] M. Karski, L. Förster, J.-M. Choi, A. Steffen, W. Alt, D. Meschede, and A. Widera, *Science* **325**, 174 (2009).
- [16] T. Groh, S. Brakhane, W. Alt, D. Meschede, J. K. Asbóth, and A. Alberti, *Physical Review A* **94**, 013620 (2016).
- [17] M. Sajid, J. K. Asbóth, D. Meschede, R. F. Werner, and A. Alberti, *Physical Review B* **99**, 214303 (2019).
- [18] C. Robens, J. Zopes, W. Alt, S. Brakhane, D. Meschede, and A. Alberti, *Physical Review Letters* **118**, 065302 (2017).
- [19] M. Genske, W. Alt, A. Steffen, A. H. Werner, R. F. Werner, D. Meschede, and A. Alberti, *Phys. Rev. Lett.* **110**, 190601 (2013).
- [20] C. Robens, W. Alt, D. Meschede, C. Emary, and A. Alberti, *Phys. Rev. X* **5**, 011003 (2015).
- [21] B. A. Bernevig, *Topological insulators and topological superconductors* (Princeton University Press, 2013).
- [22] M. König, S. Wiedmann, C. Brune, A. Roth, H. Buhmann, L. W. Molenkamp, X.-L. Qi, and S.-C. Zhang, *Science* **318**, 766 (2007).
- [23] C.-Z. Chang et al., *Science* **340**, 167 (2013).
- [24] J. Dalibard and C. Cohen-Tannoudji, *J. Opt. Soc. Am. B* **6**, 2023 (1989).

- [25] D. Steck, *Cesium d line data*, [Online; revised 14-October-2003], 1998.
- [26] D. D'oring, "Ein Experiment zum zustandsabhängigen Transport einzelner Atome" (2007).
- [27] S. Brakhane, "The Quantum Walk Microscope" (2016).
- [28] D. Jaksch, H.-J. Briegel, J. I. Cirac, C. W. Gardiner, and P. Zoller, *Physical Review Letters* **82**, 1975 (1999).
- [29] I. H. Deutsch and P. S. Jessen, *Physical Review A* **57**, 1972 (1998).
- [30] O. Mandel, M. Greiner, A. Widera, T. Rom, T. W. Hänsch, and I. Bloch, *Physical Review Letters* **91** (2003).
- [31] C. Robens, S. Brakhane, W. Alt, D. Meschede, J. Zopes, and A. Alberti, *Physical Review Applied* **9**, 034016 (2018).
- [32] M. Werninghaus, "Controlling atom transport in a two-dimensional state-dependent optical lattice" (2017).
- [33] R. P. Feynman and A. Hibbs, *Quantum mechanics and path integrals* (New York: McGraw-Hill, 1965), pp. 34–36.
- [34] A. Schreiber, K. N. Cassemiro, V. Potoček, A. Gábris, I. Jex, and C. Silberhorn, *Physical Review Letters* **106** (2011).
- [35] A. M. Childs, *Physical Review Letters* **102** (2009).
- [36] D. E. Kirk, *Optimal control theory; an introduction* (Englewood Cliffs, NJ: Prentice Hall, 1970).
- [37] T. Groh, "Fast transport of single atoms in optical lattices using quantum optimal control" (2018).
- [38] C. Robens, S. Brakhane, D. Meschede, and A. Alberti, in *Laser spectroscopy* (2016).
- [39] A. Steffen, A. Alberti, W. Alt, N. Belmechri, S. Hild, M. Karski, A. Widera, and D. Meschede, *Proceedings of the National Academy of Sciences* **109**, 9770 (2012).
- [40] N. F. Ramsey, *Physical Review* **78**, 695 (1950).
- [41] E. L. Hahn, *Physical Review* **80**, 580 (1950).
- [42] D. Steck, *Quantum and atom optics*, [Online, ver 0.12.16; revised, 23-April-2019], 2007.
- [43] A. Alberti, W. Alt, R. Werner, and D. Meschede, *New Journal of Physics* **16**, 123052 (2014).
- [44] T. A. Savard, K. M. O'Hara, and J. E. Thomas, *Phys. Rev. A* **56**, R1095 (1997).
- [45] S. Blatt, A. Mazurenko, M. F. Parsons, C. S. Chiu, F. Huber, and M. Greiner, *Phys. Rev. A* **92**, 021402 (2015).
- [46] P. Du, "Optical Intensity Control Based on Digital and Analog Systems" (2018).
- [47] M. Omar, "Atom cloud compression in a 3D optical lattice and laser intensity stabilisation using an in-house developed photodiode amplifier" (2019).
- [48] C. Robens, "Testing the Quantumness of Atom Trajectories" (2016).
- [49] E. Ippen and R. Stolen, *Applied Physics Letters* **21**, 539 (1972).
- [50] P. Russell, *Science* **299**, 358 (2003).
- [51] A. E. Siegman, *Lasers* (University Science Books, 1986).
- [52] M. Hercher, *Applied Optics* **07**, 951 (1968).
- [53] C. R. Mummerlyn and J. W. Balliett, *Applied Optics* **09**, 2535 (1970).

- [54] *Displacement behaviour*, <https://www.piceramic.com/en/piezo-technology/properties-piezo-actuators/displacement-behavior/>, Accessed: 2019-12-30.
- [55] L. B. Mercer, *Journal of Lightwave Technology* **9**, 485 (1991).
- [56] G. M. Stéphan, T. T. Tam, S. Blin, P. Besnard, and M. Têtu, *Phys. Rev. A* **71**, 043809 (2005).
- [57] G. D. Domenico, S. Schilt, and P. Thomann, *Appl. Opt.* **49**, 4801 (2010).
- [58] D. S. Elliott, R. Roy, and S. J. Smith, *Phys. Rev. A* **26**, 12 (1982).
- [59] N. Song, X. Lu, W. Li, Y. Li, Y. Wang, J. Liu, X. Xu, and X. Pan, *Applied Optics* **54**, 6661 (2015).
- [60] S. V. Shatalin, V. N. Treschikov, and A. J. Rogers, *Appl. Opt.* **37**, 5600 (1998).
- [61] M. Guizar-Sicairos, S. T. Thurman, and J. R. Fienup, *Opt. Lett.* **33**, 156 (2008).
- [62] J. Zheng, *Optical frequency-modulated continuous-wave (fmcw) interferometry* (Springer, 2005).

ACKNOWLEDGMENTS

I would like to first extend my gratitude to Professor Meschede for having the confidence in me to take on a Master thesis project in his research group and for the generosity in terms of the financial support I was provided with during my stay. The opportunity to work in the group has since proved to be extraordinarily fruitful, providing me with numerous scientific and technical challenges from which I amassed quite a lot in understanding. Above all else, it was the environment of experts and novices, from all of whom there was so much to learn from, that I will truly be eternally grateful for. Among those I would like to expressly thank first is Dr. Andrea Alberti whose ideas and direct supervision shaped my thesis. It would not have reached its final state without his input; Dr. Wolfgang Alt, whose explanations and suggestions always proved immensely insightful. I would also like to thank both Gautam and Richard, with whom I worked alongside in the lab and received most of my guidance from with regard to working with the experiment. I cannot forget to thank also the many other members of the group, who have at various times helped me by giving me valuable advice. I also thank Professor Linden for agreeing to be my second referee.

Friends and family have been so very important in weathering many a storm. I would like to thank all I have befriended and have been there to cheer me on. My parents have been my rocks throughout, their constant support in all aspects is the only reason I could make it this far. I would like to very graciously thank them as well.

DECLARATION

I hereby declare that the work presented here was formulated by myself and that no sources or tools other than those cited were used.

Bonn, 6th January 2020

Karthik Krishnappa
Chandrashekhara